universität wien

DISSERTATION / DOCTORAL THESIS

Titel der Dissertation /Title of the Doctoral Thesis

"Design and setup of a high resolution X-ray detector system to study strong interaction induced width and shift of the 1s ground state of kaonic deuterium"

verfasst von / submitted by

Carolina Berucci

angestrebter akademischer Grad / in partial fulfilment of the requirements for the degree of

Doktorin der Naturwissenschaften (Dr.rer.nat.)

Wien, 2017 / Vienna 2017

Studienkennzahl lt. Studienblatt / degree programme code as it appears on the student record sheet:	A 796 605 411
Dissertationsgebiet lt. Studienblatt / field of study as it appears on the student record sheet:	Physik
Betreut von / Supervisor:	Privatdozent Dr. Johann Zmeskal

A first measurement of kaonic X-rays (E57) is going to be performed at the K1.8BR beamline at J-PARC. The experiment aims to measure the shift and width of the K-d 1s state with an accuracy of 60 eV and 140 eV respectively. These results together with the kaonic hydrogen data will permit the determination of the isospin dependent antikaon-nucleon scattering lengths a (I=0) and a (I=1). I performed a detailed Monte Carlo study to improve the setup response in terms of S/N ratio and delivered the necessary boundaries for an optimal design of the high resolution detector. On the hardware side I worked on the characterization of Silicon Drift Detectors, which were used for a first test beam time to optimise the kaon stopping density in low density materials. In addition, the analysis of the strong interaction induced 2p shift and width (measured via the 3d$\rightarrow$2p transition) of kaonic lithium will be presented.

I would like to thank all the people who have helped me in one way or another during my time at the Stefan Meyer Institute. First I would like to express my sincere gratitude to my advisor, Johann Zmeskal, who provided support and encouragement at key times. He was always there with stimulating discussions and new suggestions, while his simultaneous enthusiasm was also much appreciated and it was essential to the completion of this work. Next I would like to thank the other members of the SIDDAHRTA collaboration, Catalina Curceanu who believed in me and gave me the possibility to join this collaboration, Micheal Cargnelli, Illiescu Mihai and Hexi Shi. Mihai's insights and differing points of view were a great help in developing new ideas and led to significant improvements in the content of this work. I owe a great debt to Hexi who gave me a important help in the final stage of my work and to Michael who has followed me since the beginning of my PhD. Finally I would like to thank my colleagues at the J-PARC lab., especially Masaharu Sato for his important support during our stay in Japan.

Contents

1 Introduction **1**

2 Kaonic atoms **3**

2.1 The exotic atoms and the kaonic deuterium scenario 3

2.2 The strong interaction in light kaonic atoms 6

2.3 The optical model 7

2.3.1 Density dependent optical potential for kaonic atoms 9

2.4 Present state-of-the-art 10

3 Experimental setup **15**

3.1 The K1.BR beam line 15

3.2 K1.8BR spectrometer system 17

3.3 E57 setup 19

4 Simulations and numerical calculations **25**

4.1 GEANT4 implementation 25

4.2 Backgrounds studies 26

4.3 MC results for the Kaonic deuterium experiment 29

4.3.1 Degrader optimisation 30

4.3.2 The trigger effect 33

4.4 Comparison MC and real data 34

5 X-ray detector **39**

5.1 The SDD working principles 39

5.1.1 The intrinsic noise and response function of the SDD 40

5.1.2 Fine structure of silicon detectors response 42

5.2 SDDs characterization during the E-57 test beam 43

5.2.1 The SDD setup 43

5.2.2 The calibration procedure 44

5.2.3 Stability studies 46

6 Kaonic Lithium measurement at J-PARC **53**

6.1 The first KLi experimental result 53

6.2 The kaons selection 54

6.3 Results 60

6.3.1 Systematic errors evaluation on K^-Li shift and width 63

7 Summary **65**

Bibliography **i**

1 Introduction

In the section which follows, an overview of the work of this thesis and how it relates to the preparation of the kaonic deuterium measurement (E57 experiment) will be given. The E57 experiment's aim is to perform a precise measurement of kaonic deuterium X-ray transition to the 1s level, such as to determine its shift and width induced by the presence of the strong interaction, in addition to the electromagnetic one.

This measurement combined with the kaonic hydrogen results, allow the extraction of the isospin-dependent antikaon-nucleon scattering lengths, which are fundamental inputs of low-energy QCD effective theories in the strangeness sector.

The K^-p interaction is now well understood from recent results of kaonic hydrogen experiments performed as KpX at KEK, DEAR and finally from SIDDHARTA at DAΦNE along with theoretical calculations based on these results. The kaonic deuterium X-ray measurement represents the most important experimental information missing in the field of the low-energy antikaon-nucleon interactions today.

The strong interaction, described by the QCD in the framework of the Standard Model, is still hiding many mysteries, especially in the low-energy limit, the so called non-perturbative regime. With the advance of the experimental techniques, both in the accelerator and detector sectors, we are presently able to perform high precision measurements, which will bring to a deeper and more complete understanding of many open questions in QCD.

Among these techniques which went through a dramatic progress in the last decades, a special place is hold by the measurements of X-rays emitted by exotic atoms. Such technique, combining knowledge in many fields, is opening the door to the understanding of physics processes going from particle physics (as chiral symmetry breaking) to astrophysics (possible role of strangeness in stars' evolution).

Exotic atoms are QED bound systems, that means any system in which a negatively charged particle, other than an electron, orbits a nucleus, under conditions in which the principal interaction with the nucleus is electromagnetic. Among the exotic atoms the kaonic ones, having a K^- replacing an e^- orbiting the nucleus, play a special role, due to the

strange quark contained in the kaon. Such atoms are providing fundamental experimental input for the study of the low energy QCD in the strangeness sector.

The electromagnetic interaction with the nucleus is very well known, therefore, even a small deviation from the electromagnetic value e.g. due to strong interaction, could be measured by performing precision experiments.

The experimental challenge of the proposed measurement is the very small kaonic deuterium X-ray yield and the difficulty in doing X-ray spectroscopy in the high radiation environment of an accelerator. A profound knowledge of each possible background source is then mandatory in order to control and to improve the signal over background ratio. A new theoretical work, giving a width of 1000 eV (most of the theoretical predictions up to now predicted values for the width between 650 to 1000 eV), which makes a detailed study of the background even more important.

Using different theoretical inputs for shift and width of the kaonic deuterium 1s state we will have all the necessary simulation tools available to study now the expected line shapes and by fitting this spectra we gain information about the possible achievable precision, dependent on the available beam time. The Monte Carlo calculation has been crucial in order to finalize the realization of the experimental setup and to proof finally the possibility to perform the kaonic deuterium experiment at the K1.8BR beam line at J-PARC.

For the detection of the 7.8 keV X-rays from the $2p \rightarrow 1s$ transitions in kaonic deuterium, 384 Silicon Drift Detectors (SDDs) will be used. These new devices have a good energy resolution and a very fast response, which allows the implementation of an external trigger in the acquisition chain, thus allowing a significant background reduction and the extraction of a very week X-ray signal.

The work is structured as follows. In chapter 2 a general overview on exotic atoms and a description of the kaonic deuterium physics is presented. The third chapter is dedicated to the description of the kaonic deuterium apparatus at the K1.8BR beam line at J-PARC hadron facility. In chapter 4 a detail explanation of the Monte Carlo techniques and results are given, while in chapter 5 a description of the X-ray detector (Silicon Drift Detectors) used by the experiment and the procedure for obtaining the K^-d X-ray spectra will be presented.

The sixth chapter presents the kaonic lithium analysis. In this work the result on shift and width is extracted using the data collected during the E57 test beam at the K1.8BR beam line at J-PARC. A preliminary study of the systematic errors is described in the last part of the chapter.

A discussion on the obtained results concludes the work.

2 Kaonic atoms

In this chapter the theoretical approach to the hadronic interaction in light kaonic atoms is reviewed. The chapter is organized in three main parts. The first one is dedicated to a short introduction to the exotic atom physics, with a focus on the Kd case. The second part presents the theoretical description of the strong interactions in kaonic atoms. A review on Deser-type formulae is followed by the description of the optical potential approach to the hadronic atoms. In the last part is shown an overview of kaonic atom experiments and theoretical work, which is constraint by our experimental results.

2.1 The exotic atoms and the kaonic deuterium scenario

An exotic atom is formed when a negative charged particle X^- is captured in an external atomic orbital. Postulated since early 40' s [1] [2], the existence of such systems was first established only in 1951 by the observation of Auger electrons from pionic and muonic silver and bromine in photographic emulsions exposed in the stratosphere on board of meteorological balloons [3]. Experimentally, an exotic atom can be produced by stopping negative hadrons such as π^-, $\overline{p}$, K^- , Σ^- in the target. During the capture process the X^- particle replaces the atomic electron by ejecting it, forming the new exotic system. The binding energies scale approximately as the ratio of the negative particle mass and the electron one (m_{X^-}/m_e). Therefore the principal quantum number n_0 where the X^- particle is captured, is given by the formula [4]:

$$n_0 = \sqrt{\frac{\mu}{m_e}} \simeq n_e \sqrt{\frac{m_{X^-}}{m_e}} \tag{2.1}$$

where n_e is the principal quantum number of the outermost electron shell. The reduced mass μ is defined as $\mu = (m_A m_H)/(m_A + m_H)$, where m_A is the nucleus mass and m_H the mass of the negative charged particle X^-. From the n_0 level the X^- will starting a series of

electromagnetic transitions towards the lower levels (quantum-cascade). The X^- particle might also be absorbed by the nucleus on its way toward the ground state.

For heavy atoms the nuclear absorption will occur from higher states and the width of these states becomes broader. The probability to reach the 1s ground state for atoms with high Z tends to zero. In Figure 2.1 an example of the cascade process of the kaonic deuterium is shown.

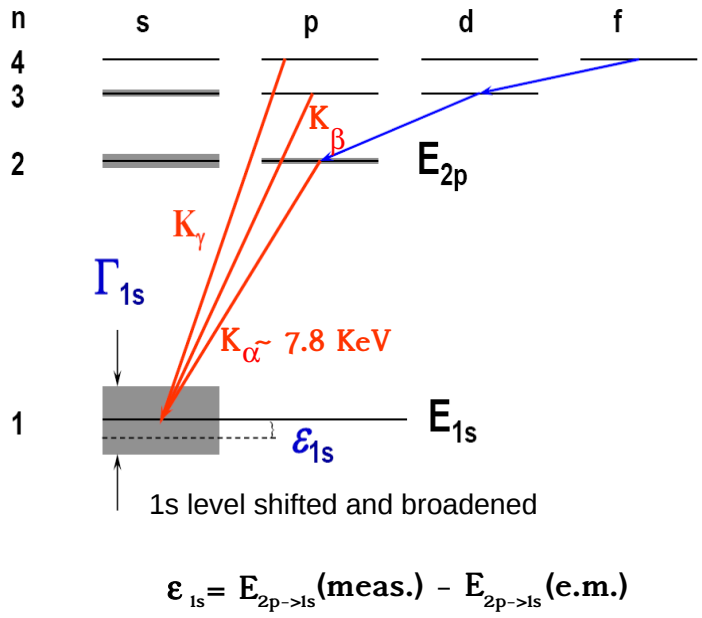

Figure 2.1: Cascade process scheme for kaonic deuterium.

The Bohr radius r_{1s} of exotic atoms is inversely proportional to the reduced mass μ :

$$r_{1s} = \frac{\hbar c}{Z\alpha\mu c^2} \tag{2.2}$$

The binding energy scales proportionally with the reduced mass μ:

$$B_n \simeq \mu c^2 \frac{\alpha^2 Z^2}{2} \tag{2.3}$$

where the symbols α, Z and n denote the fine structure constant (α^{-1} = 137.036), the nuclear charge and the principal quantum number respectively. Therefore, when the captured particle comes to lower levels (small n), the geometrical dimension of the bound system may be compared to the dimensions of a nucleus, allowing to perform a large

variety of studies. The major motivation for the hadronic atoms study is the investigation of the strong interaction at very low energies. Since the hadron-nucleon scattering processes require a low-energy extrapolation to perform such investigation, the hadronic atoms have always been fundamental in the field, because no such extrapolation is required.

The information about the strong interaction in hadronic atoms naturally emerges by comparing the transitions to low-lying bound states, given both electromagnetic and strong interactions, with the pure EM transitions very well known. The involved time scales are [5]:

- for slowing down and capture into an atomic orbit: 10^{12} - 10^{9} s
- for Coulomb de-excitation and Auger processes: 10^{12} - 10^{9} s
- for radiative transitions: 10^{17} - 10^{15} s

These processes are faster than the lifetime of the involved exotic particles, as kaons for example. Therefore, well-defined states of hadronic atom are established and the effects of the hadron-nucleus strong interaction can be studied.

For the hadronic atoms the Stark-mixing effect is quite important. Stark-mixing occurs when exotic atoms pass through the Coulomb field during collisions with other target atoms. The electric field mixes states with the same principal quantum number n, but different angular momentum. For hadronic deuterium atoms this effect is quite important because the mixing of the l-states to lower levels leads with high probability to absorption even from high n states. Stark-mixing therefore drastically reduces the X-ray yield for transitions to the lower orbits (in particular n=1, where the effect of the strong interaction is important) with increasing target density. This effect should be taken into consideration during the design phase of the experiment.

The hadronic hydrogen and deuterium give access to fundamental low energy parameters: the hadron-proton and the hadron-neutron scattering lengths respectively. The theoretical descriptions of hadronic atoms have followed different approaches developed to describe the low-energy strong interactions, in particular using the optical potential, meson exchange and the chiral perturbation theory (χPT).

Low energy phenomena in strong interaction can not be described in terms of quarks and gluons. Instead, effective field theories are used that contain the appropriate degrees of freedom to describe physical phenomena occurring at a chosen length scale, but ignore the substructure and the degrees of freedom at shorter distances (corresponding to higher energies). Chiral perturbation theory was extremely successful in describing systems like

pionic atoms, unfortunately it is not applicable for the kaonic systems. This is due to presence of resonances like the $\Lambda(1405)$, only slightly below the reaction threshold. There are however non-perturbative coupled-channel techniques based on the driving terms of the chiral effective Lagrangian which proved to be useful. They generate the $\Lambda(1405)$ dynamically as a $\overline{K}$N quasibound state and as a resonance in the $\pi\Sigma$ channel. A general feature of the theory in this field is that it relies heavily on input from experimental data. The data comes from kaon scattering experiments, atomic X-ray measurements and the energy and width of known resonances. The existing data on low energy $\overline{K}$N and $\overline{K}$N scattering are rare, poor in statistics and conflicting, furthermore the extrapolation to zero energy introduces model dependencies. The kaonic atom experiments deliver input for theory and are also tools to test the ability of theoretical models to accommodate the set of experimental values. The vividness of the field was stimulated by recent and ongoing experimental work. For some of the newer theoretical works see tab 2.1. To extract the isospin dependant $\overline{K}$N scattering lengths, in addition to kaonic hydrogen a measurement of kaonic deuterium is necessary, which is the central goal of our experiment.

2.2 The strong interaction in light kaonic atoms

In the study of strong interaction effect in kaonic atoms, the observables of interest are the shift (ε) and width (Γ) of the last observable X-ray line respect to the QED calculated values. The presence of the hadron-nucleus strong interaction, causes an energy shift (ε) and a broadening of the line, width (Γ). Line broadening is a direct measurement of nuclear absorption while the shift in energy, related to the strength of the strong interaction, is defined as the calculated electromagnetic energy minus the experimental measured energy (see Fig.2.1). Therefore the kaonic atom experiments allow to extract the effect of the strong interaction on the low-lying states by measuring X-ray transitions to these levels. The $\overline{K}$N interaction at rest is normally described in terms of complex scattering lengths, a_0 and a_1 . The experimentally determined shift and width are related to the s-wave scattering lengths at threshold. Because of isospin conservation, only the average value of the isospin I=0 and I=1 scattering lengths was obtained from the kaonic hydrogen measurement. In order to determine the isospin dependent scattering lengths, measurements of kaonic deuterium are necessary along with kaonic hydrogen data [6, 7]. To extract the isospin (I=0,1) dependent $\overline{K}$N scattering lengths, a_0 and a_1, equations (2.1) to (2.4) give the connections between the proton, neutron and deuteron scattering lengths, a_{K^-p}, a_{K^-n} and

a_{K^-d}, where m_N and m_K denote the mass of the nucleon and of the kaon, C is a correction term accommodating nuclear effects. More detail formula can be found in [8].

$$a_{K^-p} = \frac{1}{2}[a_0 + a_1] \tag{2.4}$$

$$a_{K^-n} = a_1 \tag{2.5}$$

$$a_{K^-d} = \frac{4[m_N + m_K]}{[2m_N + m_K]}Q + C \tag{2.6}$$

$$Q = \frac{1}{2}[a_{K^-p} + a_{K^-n}] = \frac{1}{4}[a_0 + 3a_1] \tag{2.7}$$

The way to correlate the complex level shift due to the strong interactions effects to the kaon-nucleon s-wave scattering length has been one of the main theoretical issue since the early '50s. The first approach to this problem is presented in the pioneering work of S. Deser et al. [9], where the study of the strong interactions contribution in light-pionic atoms is carried out.

The modified Deser formula next-to-leading order in isospin breaking is given below. The formula allows to relate the measured ε and Γ parameters to a complex scattering length [8]; where ε and Γ are recognized as the real and the imaginary part of a complex s-wave hadron-nucleon scattering length (Z=1):

$$\varepsilon_{1s} - \frac{i}{2}\Gamma_{1s} = -2\alpha^3\mu_c^2 a_{K^-d}(1 - 2\alpha\mu_c(ln\alpha - 1)a_{K^-d}) \tag{2.8}$$

where μ_c is the reduced mass of K^-d and α is the fine structure constant.

2.3 The optical model

In this section a macroscopic approach of the optical potential is described; for more details see [10]. The study of strong interaction effects in exotic atoms began with pionic atoms and is mostly related with mesons (kaons in our case). As mesons are bosons the Klein Gordon (KG) equation is used which, in the absence of a strong interaction, may be written as:

$$[-\bigtriangledown^2 + K^2 + 2mV_c - V_c^2]\psi = 0 \tag{2.9}$$

where m is the mass of the pion, $K^2 = 2mB_n$ (where B_n is its binding energy in the atom) and $V_c(r)$ is the Coulomb potential describing the interaction between the pion and the finite charge distribution of the nucleus. Then, adding for the strong interaction a potential $V_{opt}(r)$ with the condition $V_{opt}/ 2m \ll 1$, the wave equation becomes:

$$[- \bigtriangledown^2 + K^2 + 2m(V_{opt} + V_c) - V_c^2]\psi = 0 \tag{2.10}$$

A complex optical potential is necessary in order to describe absorption processes, so the binding energy acquires an imaginary component which is twice the width of the atomic state. The short ranged $V_{opt}(r)$ has strong local effects such that a perturbative approach is inadequate. The strong interaction potential can be related, at least for low density, to the hadron-nucleon forward scattering amplitude $f(0)$ and the nuclear density distribution $\rho(r)$ as

$$2mV_{opt}(r) = -4\pi F_K f(0)\rho(r) \tag{2.11}$$

where $\rho(r)$ is normalized to the number of nucleons and F_K is a kinematical factor which depends on the choice of reference frame. This equation, also known as $t\rho$ potential equation, for zero-range hadron-nucleon interaction can be written as:

$$2mV_{opt}(r) = -4\pi F_K b_0 \rho(r) \tag{2.12}$$

being b_0 equal to minus the free hadron nucleon scattering length; this value is obtained from fits to hadronic atom data and usually turns out to be different from $f(0)$ (in this case $t\rho$ potential becomes $t_{eff}\rho$ potential).

Any modification of the hadron-nucleon interaction by the nuclear medium is expected to vanish as $\rho \to 0$. If b_0 is equal to minus the free hadron-nucleon scattering length then this low-density limit [11, 12] is automatically satisfied. However, in many of the previous analysis b_0 was assumed to be independent of ρ and was found from fits to the data to be different from the free hadron nucleon value, thus violating the low-density limit. Then one needs to replace b_0 by a density-dependent function whose low-density limit is the free hadron-nucleon scattering length. A convenient macroscopic parametrization of nuclear densities is in term of 2- or 3-parameter Fermi function, which is adequate around the

nuclear surface where the r.m.s. radius is determined [13]. Outside the nucleus such distributions can't be valid since they don't have the correct exponential fall-off; in this region single particle densities or densities coming from Hartree-Fock calculations are more adequate. Since these density dependent potentials are different for each hadron, a more detailed description will be given only for the case of our interest, e.g kaonic atoms.

2.3.1 Density dependent optical potential for kaonic atoms

Strong-interaction effects in kaonic atoms are known to be non-perturbative, as evidenced by the fact that although the level shifts are repulsive, the real part of the empirical potential invariably comes out attractive ($Re(t_{eff}) < 0$). This is a direct consequence of the (absorptive) imaginary part of t_{eff} being comparable in magnitude to or larger than its real part. A purely attractive potential poses a problem in the limit of low density, where one expects [11, 12, 14] $V_{opt} \rightarrow t_{\overline{K}N}\rho$ with $t_{\overline{K}N}$ denoting the $\overline{K}$N t-matrix at threshold for which Re($t_{\overline{K}N}$) > 0, hence a repulsive potential. The clue to the low-energy K^- nuclear interactions apparently lies with the nuclear dynamics of $\Lambda(1405)$, which is commonly considered an unstable $\overline{K}$N (I = 0) bound state, some 27 MeV below the K-p threshold. Normally, $t_{\overline{K}N}$ appears repulsive due to this bound state. One then argues [15, 16] that the energy appropriate to a $\overline{K}N$ collision is shifted downward in the nuclear medium, into a regime where t $\overline{K}N$, for I = 0, appears attractive. Several model calculations [17–22] have been published in the last two decades to show how this mechanism forces the K^-nuclear optical potential at threshold to become attractive, contrary to what a naive extrapolation of the low-density limit into normal nuclear densities would give. This kind of situation, where $Re(V_{opt}(r))$ apparently contains both attractive and repulsive components, naturally suggests a non-linear density dependence of the optical potential. As an example, following E. Friedman analysis [23], the density-dependent (DD) optical potential can be written in the form:

$$2\mu V_{opt}(r) = -4\pi(1 + \frac{\mu}{m})[b + B(\frac{\rho(r)}{\rho(0)})^{\alpha}]\rho(r) \tag{2.13}$$

where μ is the K^- nucleus reduced mass, m is the mass of the nucleon and ρ(r) is the nuclear-matter density distribution normalized to the number of nucleons A. Note that for B = 0, this equation reduces to the standard $t_{eff}\rho$ parametrization of the optical potential in terms of a density-independent t_{eff} . The complex coefficients b and B, and the exponent α, can be determined by a least-squares fit to the K^- atoms data. Holding α

fixed while varying b and B to obtain a best fit to the data, repeating this procedure for a wide range of α it turns out that results can be grouped into two "families" of solutions. One family ("inflated" potentials, I), for solutions near the minimum χ^2, yields r.m.s, radii of V_{opt} larger than those of the matter density ρ, as expected from finite-range folding corrections [24]. The other family gives rise, for all its solution members, to a $Re(V_{opt})$ of spatial extent smaller than that of ρ. The latter family (of "compressed" potentials, C) offers substantially improved fits to the data, with particularly strong attraction inside the nucleus (200 $\pm$ 20MeV), about twice as strong as given by the $t_{eff}\rho$ solution.

This increased attraction supports the conjecture [25] that kaon condensation may occur, which could have deep impact also in the collapse of large stars. For some of these solutions, V_{opt} becomes repulsive at large distances, and a particular solution could be selected so that it satisfies the low-density limit $V_{opt} \rightarrow \overline{K}N\rho$. With this choice, the B $\neq$ 0 term of V_{opt}, the selected form of the potential takes in account the combined effect of embedding the energy and momentum dependence of the $\overline{K}N$ off-shell t-matrix near threshold into the nuclear medium of density ρ. Since b and B vary as a function of α, it is possible to search for a solution such that the low-density limit is satisfied.

This "nominal" solution clearly belongs to the C family; the density dependence of this solution is such that Re($Vopt$) flips its sign from repulsion as ρ(r) $\rightarrow$ 0, satisfying the low-density limit, to a strong attraction as ρ(r) $\rightarrow$ ρ(0).

Different theoretical approaches exist to describe the strong interaction at low-energies. Nowadays the most important one is the χPT. In this framework the standard QCD degrees of freedom (gluons and quarks), are shifted to the octet of light mesons and baryons in the chiral Lagrangian. Starting from the chiral Lagrangian, the scattering amplitude is evaluated by means of Bethe-Salpeter equations [18]. The scattering length is then evaluated from the calculated scattering amplitude in the standard way, by calculating its limit for the kaons momentum which goes to zero. From this point of view, the K^-p and K^-d measurements play a fundamental role in testing the the three flavour χPT.

In the case of K^-d the situation is a bit more complicated and no precise predictions have been published yet. Some recent calculations are summarized in the next section, see Table 2.1.

2.4 Present state-of-the-art

The K-p interaction is now well understood from the recent results of kaonic hydrogen obtained from KpX [26] at KEK, DEAR [27] and finally from SIDDHARTA at DAΦNE

[28] and the theoretical calculations based on these results [6, 7]. In Fig 2.2 the improved constraints on chiral SU(3) dynamics from kaonic hydrogen are shown, where the real part and imaginary part of the $K^-p \rightarrow K^-p$ forward scattering amplitude were deduced from the SIDDHARTA kaonic hydrogen measurement [7].

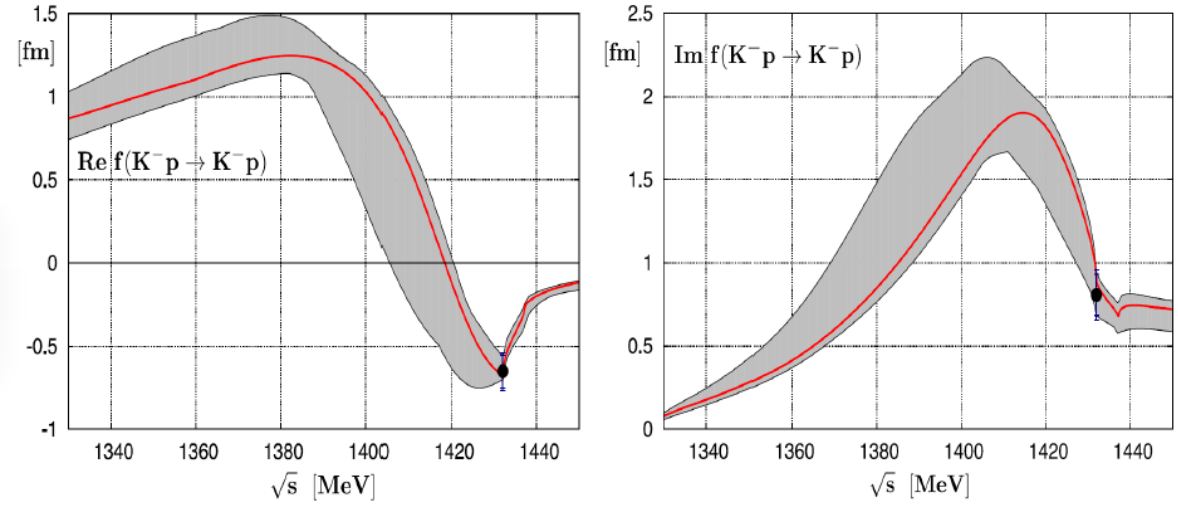

Figure 2.2: Real part (left) and imaginary part (right) of the $K^-p \rightarrow K^-p$ forward scattering amplitude extrapolated to the subthreshold region, deduced from the SIDDHARTA kaonic hydrogen measurement [7].

Recently, the most precise values of the strong interaction induced shift and width of the kaonic hydrogen 1s state were obtained by the SIDDHARTA experiment. The result of the pioneering KpX experiment together with DEAR and SIDDHARTA are shown in figure 2.3.

As we introduced in section 2.2, although the importance of kaonic deuterium X-ray spectroscopy has been well recognized for more than 30 years [29], no experimental results were obtained so far due to the difficulty of the X-ray measurement. In the latest SIDDHARTA kaonic hydrogen measurement at DAFNE in 2009, a first exploratory kaonic deuterium measurement was also made.

The analysis of the kaonic deuterium data delivered a 1.7 σ hint of a signal, if the values for shift and width of the K-series transition are taken from theory: shift = -800 eV and width = 750 eV. The upper limits for the yield of the K$-$series transitions were derived in this analysis: $Y(K_{tot}) < 0.0143$ and $Y(K_\alpha) < 0.0038$ (CL 90%). In Fig. 2.4 a fit of the kaonic deuterium X-rays lines is shown.

On the theoretical side, there are many recent publications predicting values of the shift and width for the kaonic deuterium 1s state. In Table 2.1 are collected the values of last theoretical calculations.

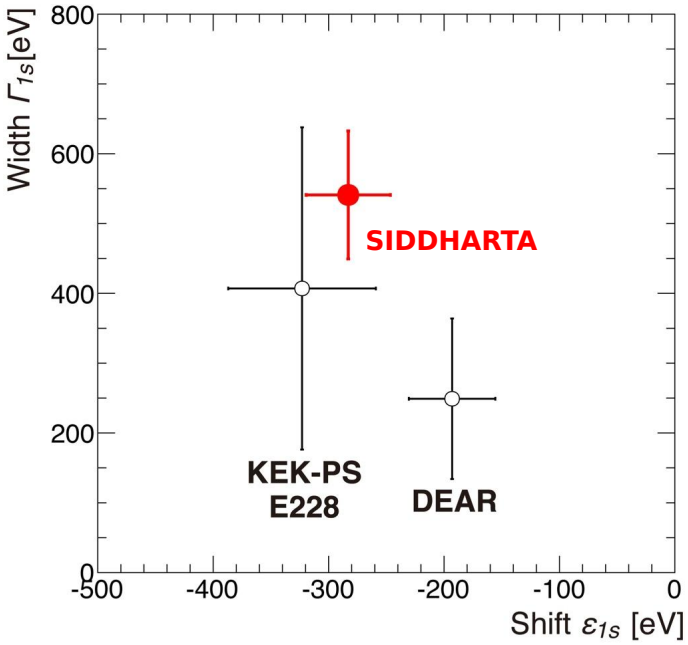

Figure 2.3: Comparison of experimental results for the strong interaction shift and width of the kaonic hydrogen 1s state.

a_{k-d} [fm]	ϵ_{1s} [eV]	Γ_{1s} [eV]	ref.
−1.55+ i 1.66	−969	938	Weise 2015 [31]
−1.58+ i 1.37	−887	757	Mizutani 2013 [32]
−1.48+ i 1.22	−787	1011	Schevchenko 2012 [33]
−1.46+ i 1.08	−779	650	Meißner 2011 [6]
−1.42+ i 1.09	−769	674	Gal 2007 [34]
−1.66+ i 1.28	−884	665	Meißner 2006 [35]

Table 2.1: Compilation of predicted K^-d scattering lengths a_{k-d} and corresponding experimental quantities ϵ_{1s} and Γ_{1s} (taken from [36]).

“The most recent cascade calculations for kaonic deuterium are shown in Fig. 2.5, where the X-ray yields per stopped kaon for K_α-, K_β- and K_γ-transitions in a wide density range were calculated. As input in our Monte Carlo simulation we used a K_α-yield of 0.1% for the gas targets and 0.01% for the liquid target, which are between the calculated values of Koike [37] and Jensen [38]" [39].

In K^-d the Stark mixing is one of the main “loss" processes (see paragraph 2.3). These collisional processes are caused by the interaction of the K^-d atom with the neighbouring atom/molecules of the target.

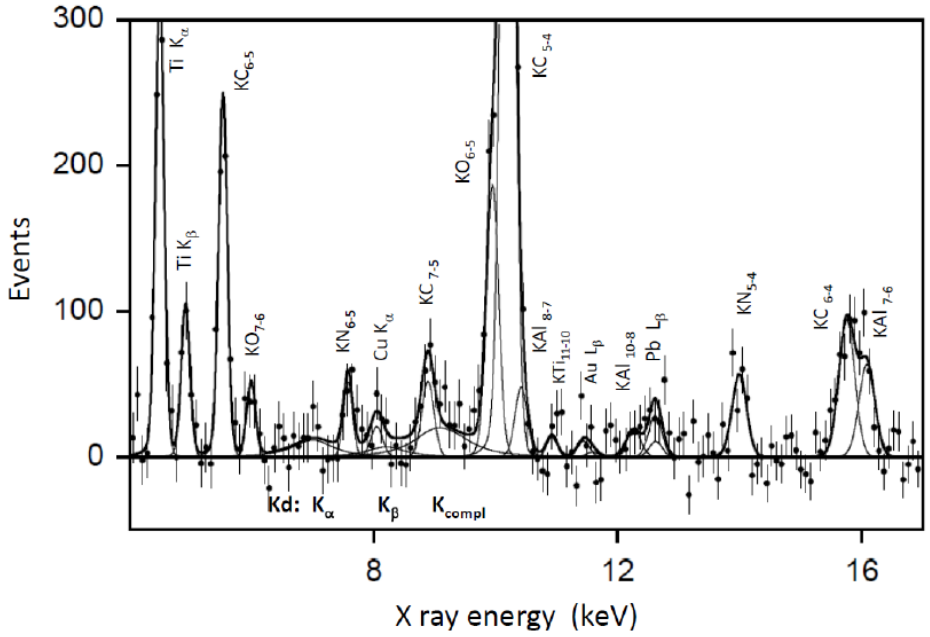

Figure 2.4: Example of a fit of kaonic deuterium X-ray lines. "X-ray spectrum from the kaonic deuterium experiment. Fit with fixed Kd transition shift and width (-805, 750 eV) and fixed yield ratio of the individual K-transitions. Integrated luminosity 100 $pb^{-}1$. The lines from kaonic X-rays due to stops in the window foils and from X-ray fluorescence excited by background are labeled" [30].

Therefore their contributions can be minimized by enhancing the mean free path of the exotic atom in the target. The use of a gaseous target enhances the $K^{-}d$ mean free path, minimizing the competitor processes contributions, but at the same time reduces the stopping power of the target, lowering the capture cross section. It is therefore necessary to find an optimum value for the target density, which takes into account the yield calculation. Indeed if the density is too high, the $K^{-}d$ X-ray yields would become smaller due to the Stark mixing (see paragraph 2.1) and the signal over background ratio would become worse. Otherwise, if the target density is too low, the capture-cross section would be too small and the signal over background is still worse. Finally a density of 5% of LDD was chosen as a good compromise taking into account all the physical processes described above.

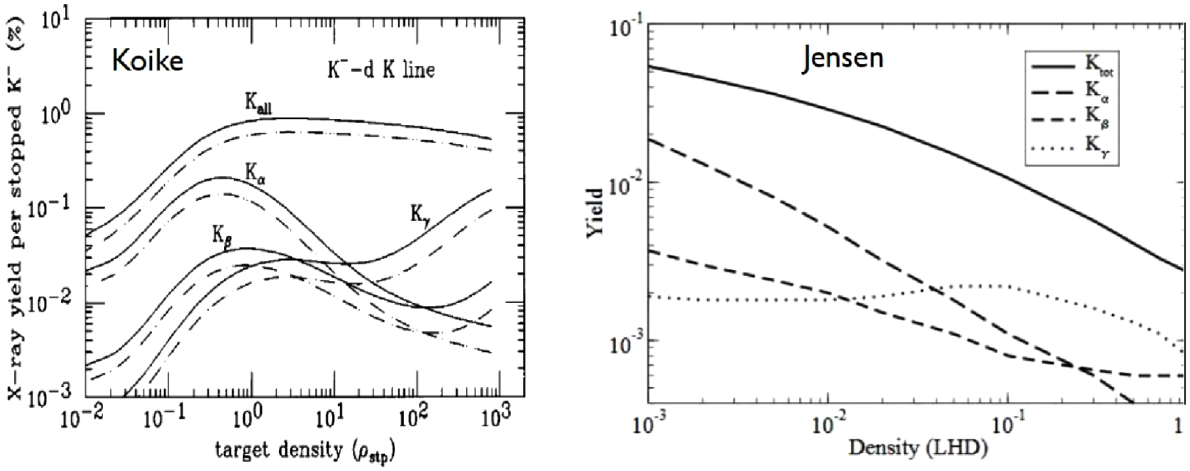

Figure 2.5: Kaonic deuterium cascade calculations, for the X-ray yield of K_α, K_β, K_γ and K_{tot}; figure from reference [37] (left) and from [38] (right).

3 Experimental setup

Japan Proton Accelerator Research Complex (J-PARC) constructed by KEK and Japan Atomic Energy Agency is a high intensity proton accelerator facility. There are three experimental facilities, Material and Life science Facility (MLF), Neutrino experimental facility and Hadron experimental facility. The proposed kaonic deuterium experiment will use the excellent features of the K1.8BR kaon beam line together with the K1.8BR spectrometer at the hadron experimental facility.

3.1 The K1.BR beam line

The J-PARC facility consists of three proton accelerators, a 400 MeV linac, a 3 GeV rapid cycle synchrotron which provides the beam to MLF, where secondary beam of muons and neutrons are used, and a 30 GeV main ring (MR) synchrotron. MR produce a fast extraction beam to produce a neutrino beam to the neutrino experimental facility or a slow extraction beam to the hadron experimental facility.

The K1.8BR beam line was designed to obtain a high-intensity kaon beam up to 1.2 GeV/c. The configuration of K1.8BR beam line is shown in Fig. 3.1 and its parameters are summarized in Table. 3.1. The K1.8BR beam line branches off from K1.8 at a bending magnet downstream of an electrostatic separator, ES1, used to purify secondary beams of charged particles with momenta up to 1.2 GeV/c in the K1.8BR beam line. K1.8BR has a rather long length of 31.3 m from the production target (T1) to the final focus point (FF), where the experimental target will be set. Its length optimizes the transport of low-momentum kaons, and a 6-m-long Electrostatic Separator (ESS1), together with Correction Magnets (CM) and vertical slits (IF-V, MS1), has excellent particle separation power. By adjusting the gap distance between IF and MS1, the kaon intensity and the K^-/π ratio at the final focus point of the spectrometer are successfully controlled.

The beamline tuning plays an essential role for a stopped experiment. A negative kaon beam tuning was successfully done at 0.7 GeV/c and 0.9 GeV/c during the test beam

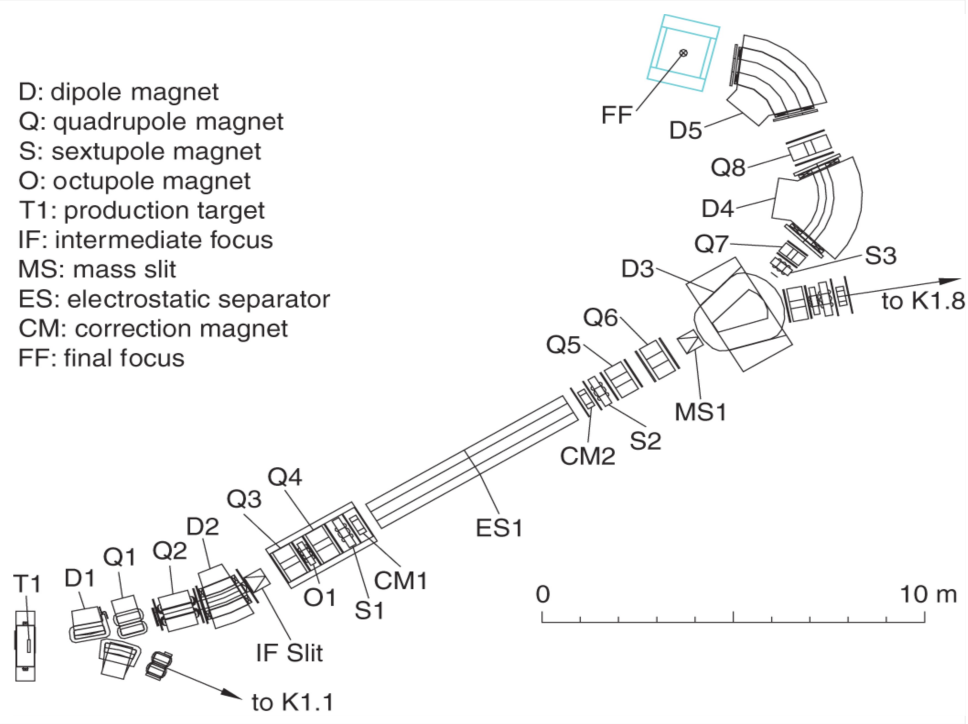

Figure 3.1: Configuration of the K1.8BR beam line in the hadron hall of J-PARC [40].

in June 2016. Hardware online triggers for beam particles had been established and the beamline study is well under way. Dedicated studies of optic, acceptance of beamline ESS1 and slits, particle yields against momentum and central momentum of the beamline at the K1.8BR has been done, and feasibility of high-precision kaonic atom x-ray spectroscopy with SDDs has been demonstrated. This beam tuning run has shown in fact, that we are ready to stop kaons for the E57 experiment (see paragraph 4.4). More details of the beam line, such as the beam line elements and optical design, are described in Ref. [40].

Primary beam	30 GeV/c proton
Secondary beam	0.7 - 0.9 GeV/c K^-
Repetition cycle	6 sec
Flat top	2.93 sec
Production target	Pt (50% loss) / Ni (30% loss)
Production angle	6 degrees
Length (T1-FF)	31.3 m
Acceptance	2.0 $msr \cdot \%(\Delta\Omega \cdot \Delta p/p)$
Momentum bite	$\pm 3\%$

Table 3.1: Parameters of the K1.8BR beam line [40].

3.2 K1.8BR spectrometer system

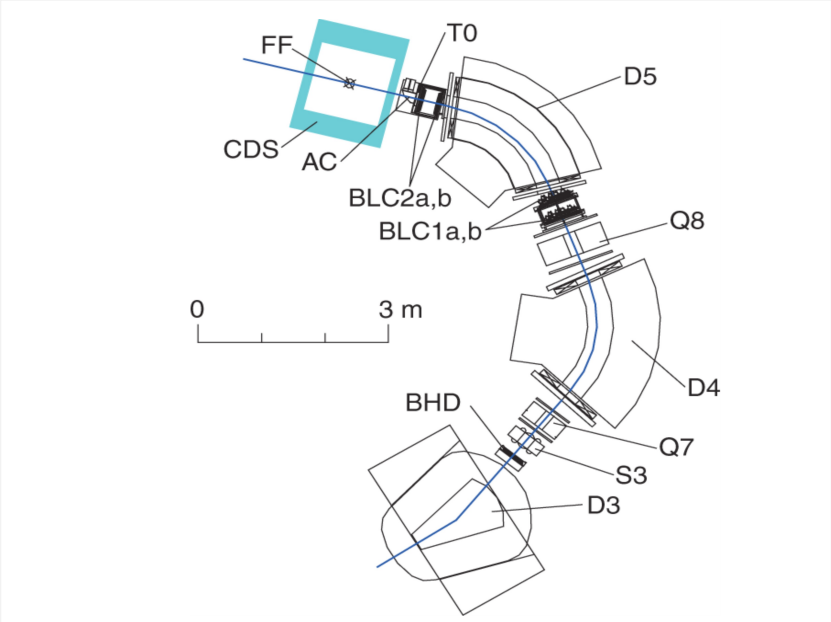

Figure 3.2: Schematic view of the beam line spectrometer. The setup consists of a beam line spectrometer, a cylindrical spectrometer system (CDS), trigger counters (BHD and T0), beam line chambers (BLC1 and BLC2), and a kaon identification counter (AC). The beam line magnet, composed of an SQDQD system, consist of beam sweeping dipole magnets (D4 and D5), quadrupole magnets (Q7 and Q8) and a sextupole magnet (S3) [40].

The beam line spectrometer (Fig. 3.2) is composed of beam line magnets, trigger counters, beam trackers, and a kaon identification counter. The beam line magnets, composed of an SQDQD system, are located downstream of a branching magnet D3. The beam trigger is a coincidence signal from two trigger counters located downstream from magnets D3 and D5, separated by a 7.7 m flight path. Kaon beams ranging in momentum from 0.7 to 1.2 GeV/c are identified with the kaon identification counter. Pions in the beams are discriminated from kaons using the kaon identification counter, and protons are removed by ES1. The trajectory of the kaon beam is tracked with the two beam line chambers installed across the D5 magnet.

The kaon momentum is analyzed using this tracking information together with beam optics of the D5 beam line magnet to attain an expected momentum resolution of 0.1%. At the down stream of the D5 magnet, particles were detected by the T0 counter and Defining counter (see Figure 3.5) together with tracking information provided by the beamline drift chambers (BLC1 and BLC2). In addition an energy measurement counter (E0), located downstream of the degrader, is used in the beam trigger. The E0 detector consist of 3

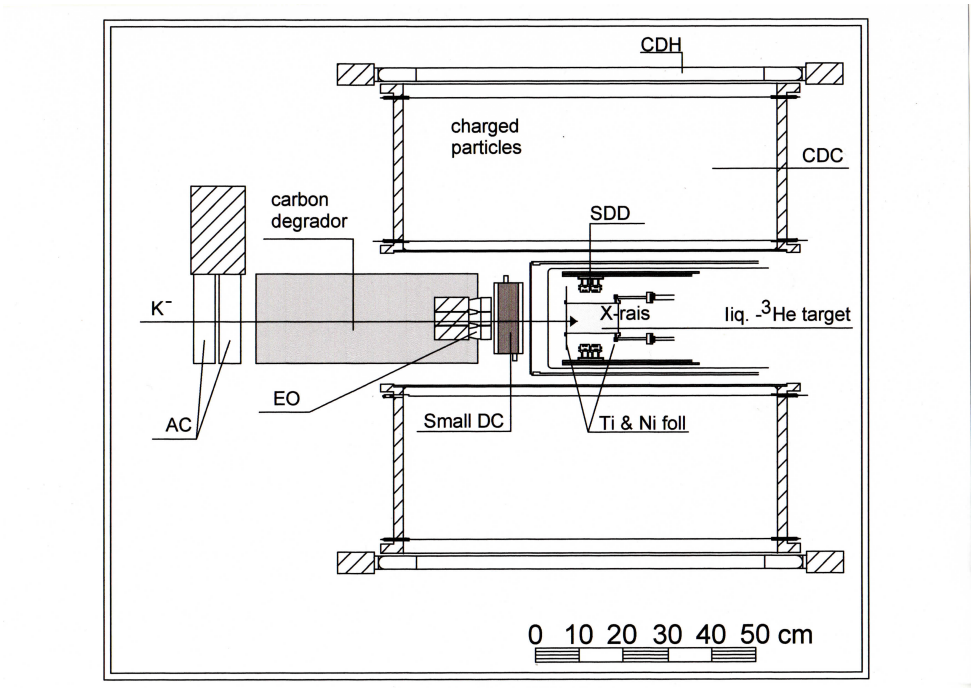

Figure 3.3: E17setup.

segmented plastic scintillation counters (EJ-230). Each scintillator has a 100x30 mm^2 surface and is 20 mm thick, see Fig. 3.4. It is readout by fast photomultipliers (PMT, Hamamatsu 6151-01B) which signals are processed by TDC units. The aerogel Cherenkov (AC) counter (n = 1.05), located downstream of the T0 counter is used for an On-line pion identification on the first trigger level. The AC has an effective area of 166 mm (width) × 166 mm (height) × 50 mm (thickness).

The T0 counter consists of 5 segmented scintillator bars (Fig. 3.5 (a)). Each segment has 16 cm (vertical) and 3.2 cm (horizontal) effective area with a thickness of 1 cm. Two PMTs, HAMAMATSU 6612B, with three-stage boosters are mounted on both ends of each scintillator. The T0 counter will be used to determine the timing of beam triggers. To suppress the trigger rate, we prepared an additional beam defining counter (Fig. 3.5 (b)) just in front of the target chamber. The plastic scintillator (BC420) is 1 cm thick and has the size of 12 cm (vertical) 12 cm (horizontal), which just covered the foil positions inside the target chamber. One PMT, HAMAMATSU 6612B with three-stage boosters is attached on it. The kaon beam is tracked with two beam line chamber (BLC1 and BLC2), which are planner drift chambers consisted of 8 layers, while the secondary charged particles are detected by the Cylindrical Detector System (CDS) which covers $\sim$ 60 % solid angle with a cylindrical drift chamber (CDC) and scintillation hodoscope counters (CDH). These detectors enables us to select X-rays originated only in the target volume.

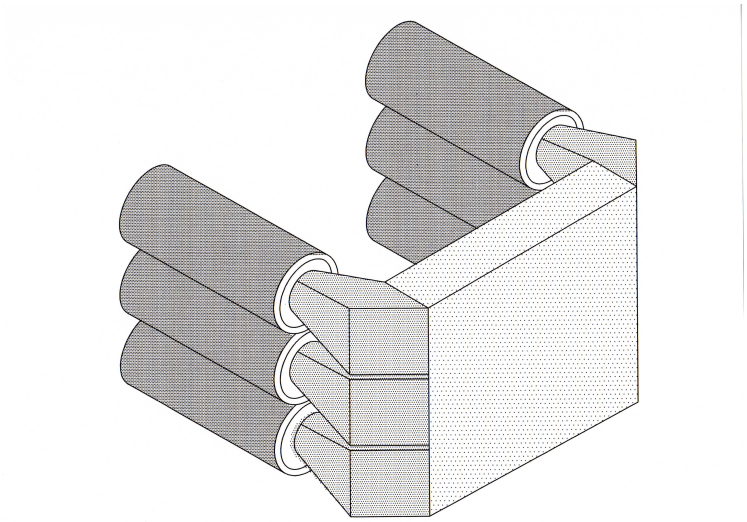

Figure 3.4: E0 detector. The E0 detector consist of 3 segmented scintillator bars (EJ-230). Each segment has 30 mm (vertical) and 100 mm (horizontal) and 20 mm (thickness). Six PMTs, HAMAMATSU (6151-01B) are mounted on both ends of each scintillator.

"The cylindrical drift chamber, with a diameter of 1060 mm and length of 950 mm, is surrounded by a cylindrical detector hodoscope (CDH) to trigger on decay particles. The proposed setup will allow the tracking of the incoming kaons with segmented plastic scintillators as start counter and the beam line chamber (BLC) for tracking. The produced charged particles due to kaon absorption on the nucleus will be tracked by the large cylindrical drift chamber (CDC), while the cylindrical detector hodoscope (CDH) is used as trigger. These parts of the experimental setup will be utilized for the E57 experiment and it will be upgraded with a cryogenic target system and a X-ray detector system with a total area of 246 cm^2" [39].

3.3 E57 setup

For the E57 experiment we plan to use the J-PARC K1.8BR multi-purpose spectrometer (see Fig. 3.6), which has quite unique feature for our needs, namely a large acceptance cylindrical drift chamber (CDC) for charge particle tracking, necessary for efficient background reduction for the proposed study of kaonic deuterium X-rays. The kaonic deuterium setup will be similar to the E17 experimental setup (Fig. 3.3). The E17 experiment proposes to measure the strong-interaction shift of 3d→2p X-rays of kaonic helium-3 atoms with a precision of 2 eV. For the kaonic deuterium measurement, we propose to upgrade the spectrometer with a cryogenic deuterium target surrounded by Silicon Drift Detector

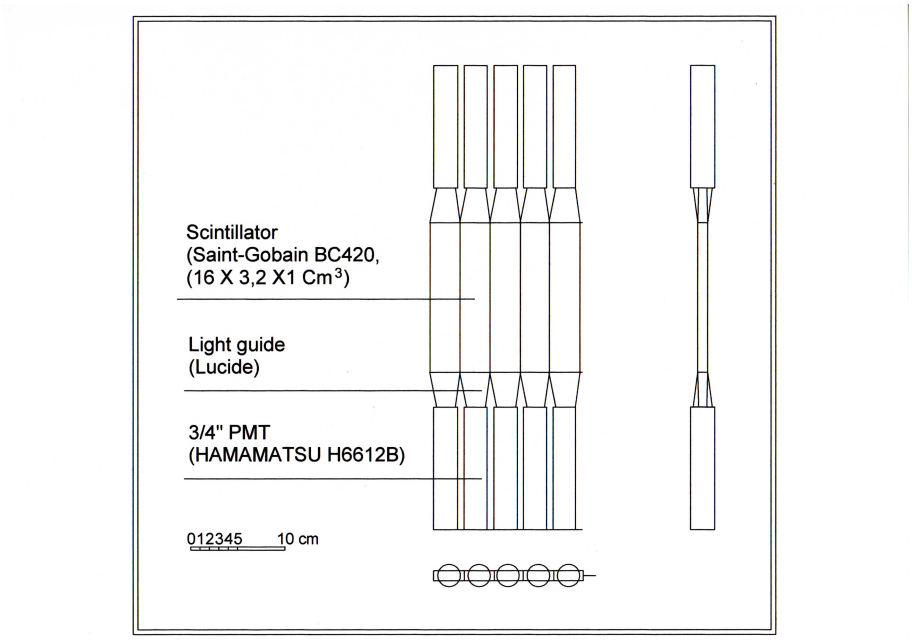

(a) T0 counter

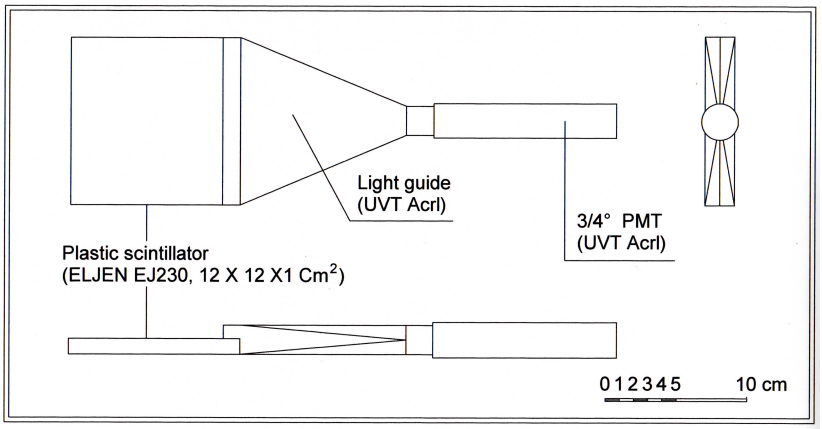

(b) Define counter

Figure 3.5: Trigger counters.

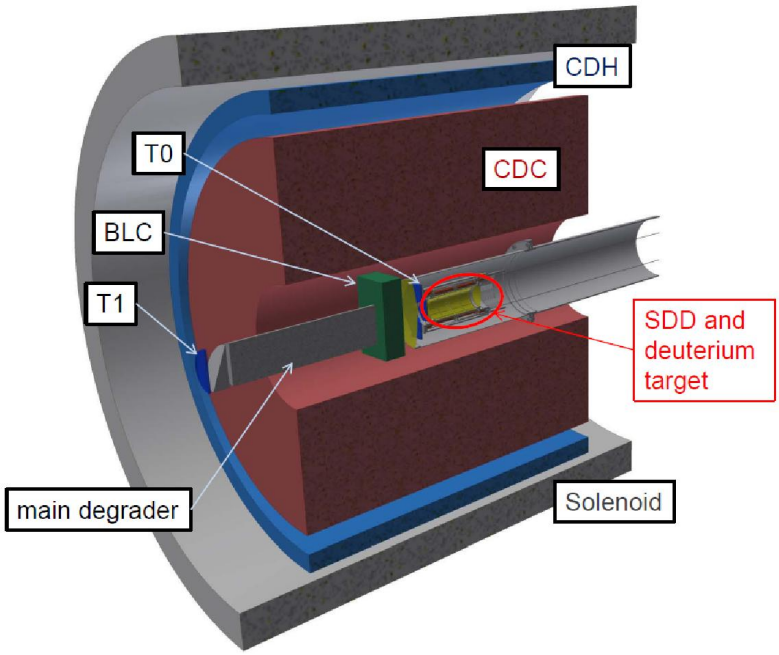

Figure 3.6: E57setup at the K1.8BR.

(SDD) with a total area of 246 cm^2 for the KD X-ray detection. “The cryogenic target cell will be made of a 75 μm Kapton body with a diameter of 65 mm and a length of 160 mm, with reinforcement structure made out of aluminium. In addition, the cooling and mounting structure of SDDs is used to reinforce the target cell in longitudinal direction. The working temperature of the target cell is around 30 K with a maximum pressure of 0.35 MPa. With these parameters, a gas density of 5% liquid deuterium density (LDD) will be achieved" [39].

Finally 48 monolithic SDD arrays (384 single elements) will be structured close together around the target, as illustrated in Fig. 3.8. Each monolithic array is 450 μm thick and consist of eight square SDD units, each with an active area of 8x8 mm^2. These individual SDD units are arrange in a 2x4 array format with a 1 mm dead area along its border (total area 18x34 mm^2). One such SDD array can be seen mounted on Alumina ceramic carrier. The ceramic carrier is later assembled on top of an Aluminum holder block using M1 screws as shown in Fig. 3.7 (bottom). This block not only protects the delicate detector bonding connections but also assists in cryogenic cooling of the SDD array. For each SDD unit, an integrated charge sensing amplifier CUBE is placed in close proximity of the SDD anode to be electrically connected to ceramic carrier using bonding wires (Fig. 3.7 top) [41]. The “CUBE” preamplifier chips will be essential for the success of the proposed experiment. with the possibility to build a device with an excellent ratio of active to total

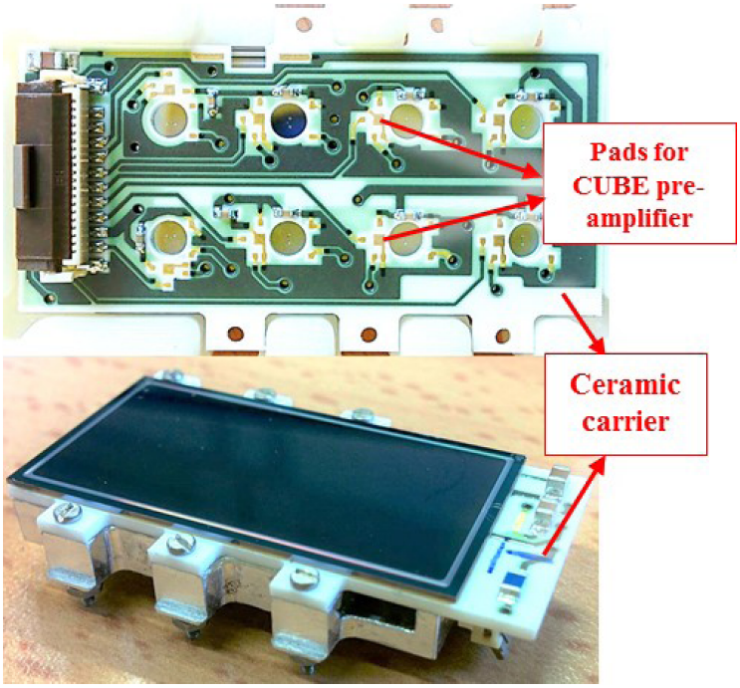

Figure 3.7: "Monolithic array of eight 64 mm^2 SDD units. The ceramic carrier can be seen with holes to facilitate bonding of the SDD units and placement of charge pre-amplifiers (Top). The SDD array is mounted on a ceramic carrier which is further assembled on Aluminum holder with M1 screws (Bottom)" [41].

area of 85%, which allows a high packing density around the target cell to cover a large solid angle of about 2π. And, the additional feature of these SDDs to achieve a timing capability in the order of 100 ns, while keeping the excellent energy resolution of the device, is important for the necessary background reduction. More details about SDD and the first test result at the J-PARC K1.8BR spectrometer are described in chapter 5.

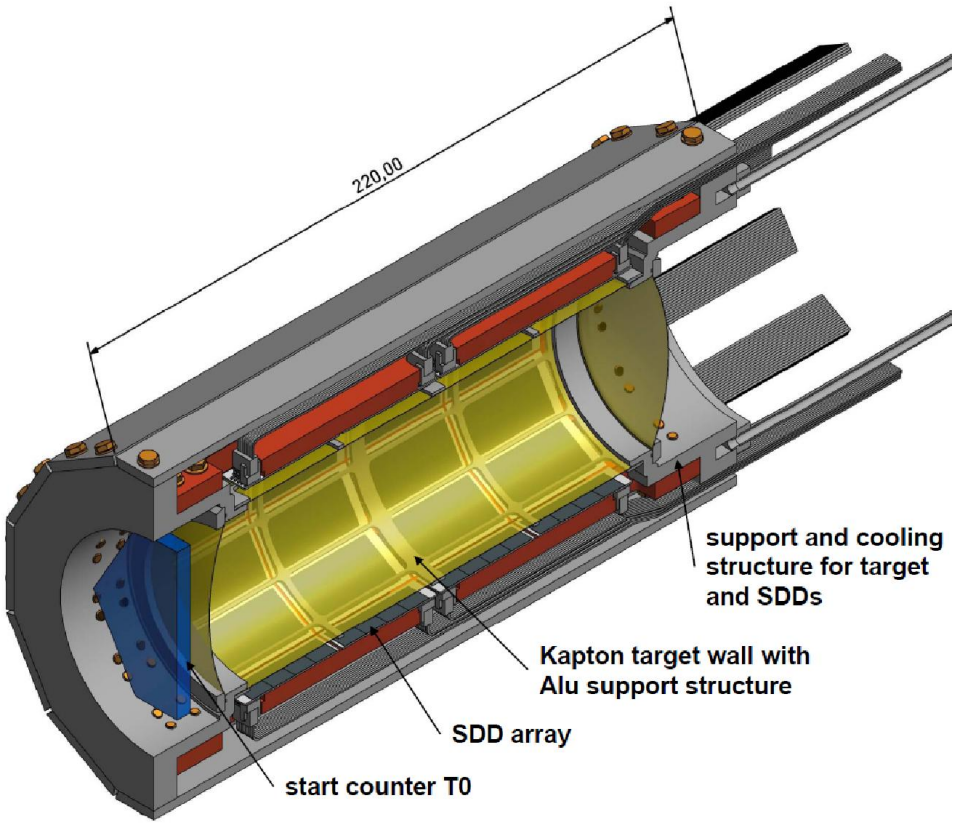

Figure 3.8: Design of the cryogenic target and X-ray detector system.

4 Simulations and numerical calculations

Monte Carlo simulations have become essential when developing new equipment, providing substantial cost savings on prototyping and design work. Such simulations also provide a method to improve understanding of existing processes, and of critical points in an experimental setup. For this purpose, the program is used to optimise the main parameters of the setup, like target, detectors configuration and degrader geometry, for the higher target gas density to be used in the E57 experiment. The structure and the composition of different material out of which the setup are built were reproduced with high accuracy, particular attention being given to the low energy detectors (SDD) mounting, to the tracking and degrader devices.

4.1 GEANT4 implementation

The GEANT4 package was chosen for the task, with special care on the low energy tools. Low energy electromagnetic physics models (valid from 250 eV - 100 MeV) are used to model photon interactions with materials throughout all the simulations. This is implemented via a modular physics list, which uses the built–in GEANT4 particle definitions. This includes common bosons, leptons, mesons, baryons and an ion constructor.

The low energy electromagnetic processes were simulated using the Livermore model, which allows particle tracking down to few keV and moreover, reproduces well the fluorescence photons, Auger emission and Photon Induced X–ray Emission (PIXE). Within the physics list, all available electromagnetic processes are defined, as well as transportation through the geometry, radioactive decay, and a stepping process. The class stopping manager in Geant4 plays an essential role in tracking the particle. It takes care of all message passing between objects in the different categories relevant to transporting a particle, for example, geometry and interactions in matter.

The exotic atom formation and the nuclear absorption on deuterium cannot be simulated using standard GEANT4 class libraries; moreover, the introduction of a beam simulated externally (with an accelerator-specialized Monte Carlo) in the GEANT particle generator is not fully compatible with the standard "ParticleGun" class nor with the extended GeneralParticleSource one [G4phys]. We had to modify the code in order to introduce in the simulation the background coming from the lost particle in the beam line. An external beam of pion was included, particle per particle, each having its own coordinate, momentum and weight, see Figure 4.3.

Therefore, several basic libraries have been enlarged to better describe the low energy kaon physics. The low energy hadronic interaction package was activated for nuclear interactions, for what concerns the nuclear absorption of the stopped kaons, as final step of the atomic cascade, the radiative transitions of most of kaonic atoms were included, with tunable yields, to simulate both signal (deuterium X-rays) and structured background (characteristic X-rays lines of other kaonic atoms).

Particularly with regard to the nuclear absorption of the stopped kaons as final step of the atomic cascade, the existing library (G4KaonMinusAbsorptionAtRest) lacks completely the channel involving a single nucleon. Therefore, deuterium is considered only as electromagnetic scattering medium, but behaves like vacuum on the strong interaction side.

Since one of the main goals of the experiment is the kaonic deuterium measurement, an appropriate treatment has been included, by removing the Fermi motion and conserving all compatible channels. In addition to that, the radiative transitions of most of kaonic atoms were included as well, with tunable yields, to simulate both signal (kaonic hydrogen and deuterium X-rays) and structured background (characteristic X-rays lines of other kaonic atoms).

4.2 Backgrounds studies

To improve the setup response in terms of signal over background, which represents the main request for measuring the K lines of the kaonic deuterium atoms, a detailed study of the backgrounds sources was developed.

The reduction of this background will be done by eliminating the major sources, identified by Monte Carlo, reducing the number of inefficient triggers and fastening the SDD time response by cooling the SDDs to lower temperature.

There are two types of background sources; correlated (synchronous) and uncorrelated (asynchronous) to the incoming K^-. While the "hadronic" (synchronous) background is

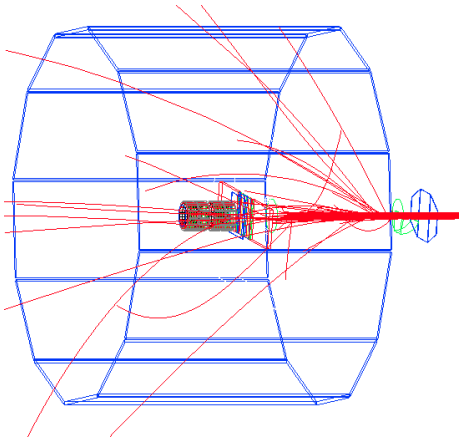

Figure 4.1: Monte Carlo configuration of the E57 experiment (side view). The simulation covers the full focal point region, up to the T0 scintillator. The red tracks are kaons of 0.7 GeV/c momentum.

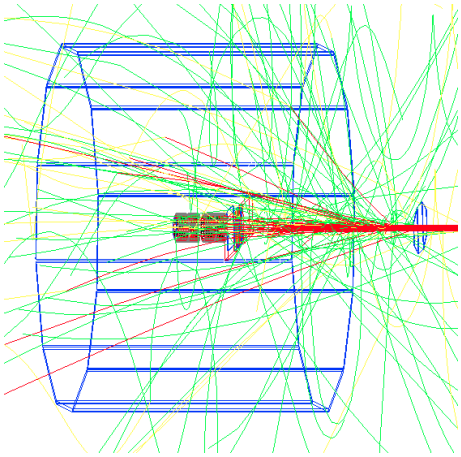

Figure 4.2: Same configuration with kaons of 0.7 GeV/c momentum in red, pion in green and muon in yellow.

a direct result of the K^- related processes like kaon atomic cascade, nuclear absorption and decay, the asynchronous one comes from the accelerator lost particles which develop showers in the elements of the setup and in the mechanical parts of the SDD mounting.

In the simulations done for E57, synchronous and asynchronous background were simulated. It was assumed that the background originates from hits of charged particles and high energy γ-rays which partly come from accidental beam particles, and partly in coincident from secondary particles emitted after K- absorption in deuterium.

In order to maximize the signal, the kaon moderation, capture and cascade processes were followed in the MC. After being degraded by properly shaped carbon and copper layers, the kaons are slowed down by ionization and excitation of the deuterium molecules, until their energy is low enough to get captured into an atomic orbit with a high principal quantum number.

The exotic atom then cascades down via Coulomb de-excitation and external Auger processes until reaching the lower lying states, where the probability for radiative transitions becomes dominant. The odds for kaons to reach 1s ground state and be absorbed by a nucleus, are reduced by the Stark mixing effect which, in turn, depend on the target density.

A density of 5% liquid deuterium density (LDD) has been chosen, granting a good compromise between Stark mixing and kaon stopping yield. The list of kaon nucleon absorption rates and kaon decay channels dominated are summarized as follows:

- K^- absorbed by a proton :
  - $\Sigma^-\pi^+$
    - $(n\pi^-)\pi^+$ (100%)
  - $\Sigma^+\pi^-$
    - $(p\pi^0)\pi^-$ (52%)
    - $(n\pi^+)\pi^-$ (48%)
  - $\Sigma^0\pi^0$
    - $(\Lambda\gamma)\pi^0$ (100%)
      - $((p\pi^-)\gamma)\pi^0$ (64%)
      - $((n\pi^0)\gamma)\pi^0$ (36%)
  - $\Lambda\pi^0$
    - $(p\pi^-)\pi^0$ (64%)
    - $(n\pi^0)\pi^0$ (36%)
- K^- absorbed by a neutron:
  - $\Sigma^-\pi^0$
    - $(n\pi^-)\pi^0$ (100%)
  - $\Sigma^0\pi^-$
    - $(\Lambda\gamma)\pi^-$ (100%)
      - $((p\pi^-)\gamma)\pi^-$ (64%)
      - $((n\pi^0)\gamma)\pi^-$ (36%)
  - $\Lambda\pi^-$
    - $(p\pi^-)\pi^-$ (64%)
    - $(n\pi^0)\pi^-$ (36%)

As can be seen, most of the channels include a charged pion. The emitted pion has enough energy to pass through the SDD cooling system, electronics and vacuum chamber, eventually reaching the cylindrical detector hodoscope placed around the setup.

In order to provide a more realistic simulation an external beam of pions, which represent the main contribution of accelerator background, has been included in the MC. Figure 4.3 shows the pion profile taken during the run at the K1.8 BR in April 2015. The input for the MC, consists of position, weight and momentum distribution of the pions leaving the beam pipe at T0. That pion external beam was then inserted and used for the machine background calculation.

Processes create particles hit SDD (Energy deposit in SDD : 1keV< dE< 20 keV)	Particles hit SDD
primary (products of K^- abs.) 15.3%	π^-(73%),π^+(15%), p(6%), n(6%)
Ionization by hadron 72.1 %	e^-(100%)
Ionization by e^- 3.4 %	e^-(>99%),γ
bremsstrahlung 8 %	γ(100%)
decay of secondary particles 0.9 %	γ(63%),μ^-(11%),e^-(17%),e^+(9%)
ionization by muon 0.2	e^-(100%)

Table 4.1: sources of background.

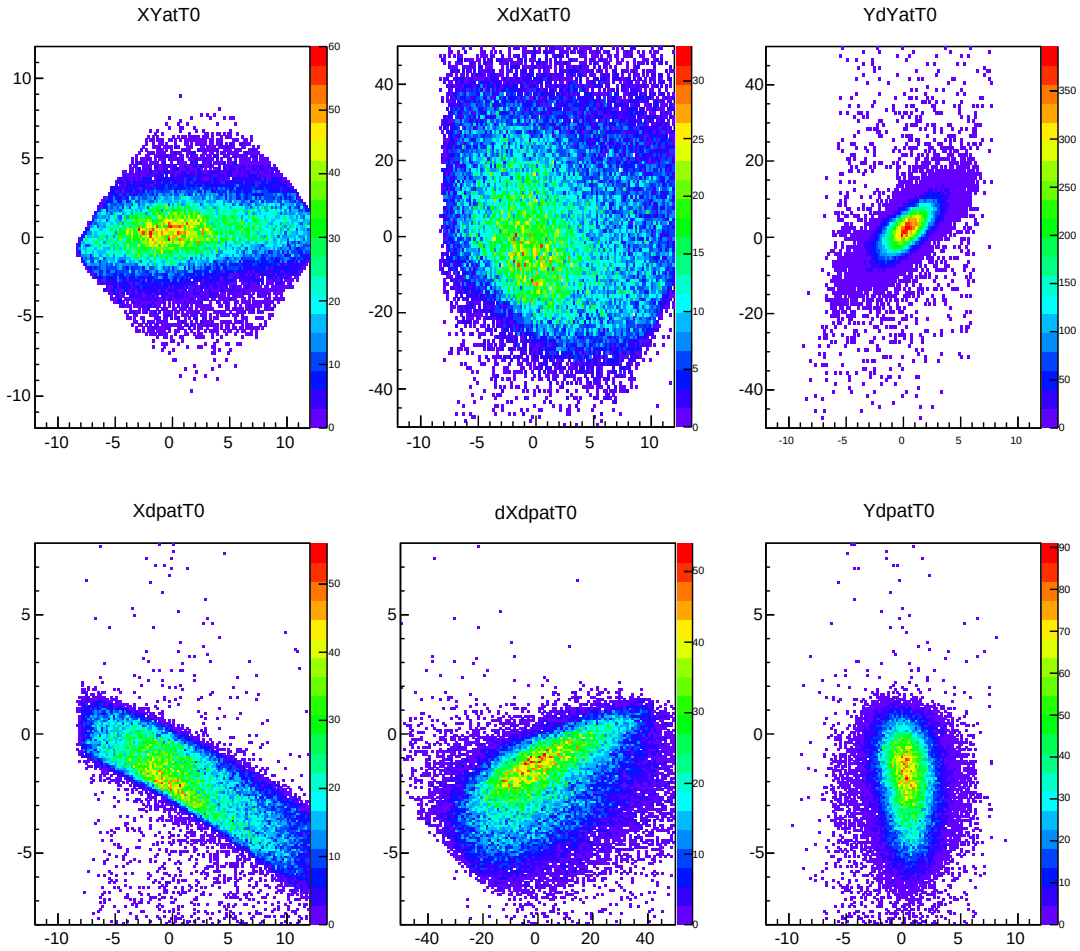

Figure 4.3: Beam profile of the pions at T0 counter (130 cm upstream of final focus). The cross sections of perpendicular directions to the beam axis are shown (top). Position dependence of the momentum (bottom.)

In the Table 4.1 are summarized the total particles hitting the SDD detectors. According to the Monte Carlo physics package, the low-energy electrons from ionizations by hadron (pions, proton) are the dominant background source.

4.3 MC results for the Kaonic deuterium experiment

The simulations starts at the T0 counter with $2{\cdot}10^9$ K^- of 700 MeV/c kaons with +-3% (flat) momentum bite (Fig. 4.2). The beam properties were taken during the beam time of E15 (Run 62) at the K1.8 BR in April 2015. The kaon production rate was measured at 24 kW proton beam power, at three kaon momenta 0.9 GeV/c, 1.0 GeV/c and 1.1 GeV/c. The

old measurements with kaon momenta from 0.7 GeV/c to 1.0 GeV/c were normalised to the new measured values.

- produced kaons per spill for a proton beam momentum of 1 GeV/c
  normalised to 1 kW $\longrightarrow$ 5000 kaons/spill (kW)
  with a K^-/π^- ratio $\longrightarrow$ 45 : 100

- produced kaons per spill for a proton beam momentum of 0.7 GeV/c
  normalised to 1 kW $\longrightarrow$ 500 kaons/spill (kW)
  with a K^-/π^- ratio $\longrightarrow$ 5 : 100

Typical K^- intensity and K^-/π ratio for the 1.0 GeV/c negative beam are achieved as 10 k/spill/kW and 0.3, respectively, as shown in Fig. 4.4. This K- intensity lies between the estimations by the Sanford–Wang formula with and without kinematic correction.

In the following MC simulation I use as input a kaon yield of 500 per spill and kW at a momentum of 0.7 GeV/c (see Fig. 4.5).

4.3.1 Degrader optimisation

"For use as a kaon degrader, several materials (carbon, copper, polyethylene and iron) were compared during the simulation. The highest stopping rates for 0.7 GeV/c kaon beam were obtained with a carbon degrader of about 40 cm thickness" [39]. Figures 4.6 (a) and (b) show the kaon stopping distribution in beam direction, as can be seen, 90% of kaons are stopped in the degrader. In Table 4.2 the optimised results for the carbon degrader thickness are summarised for a gaseous and for a liquid target. Even if the stopping rate is higher for the liquid case, a density of 5% LDD has been chosen as optimum according to the yield estimation which is supposed to be a factor 10 higher than for the liquid case.

Degrader thickness [cm]	Kaon target stops per beam kaon (10^{-3})	Target density
40	0.31	0.03
40	0.50	0.05
39	9.5	1

Table 4.2: "Kaon stopping density in gaseous and liquid targets, optimised for carbon degrader. The target density is given relative to the liquid deuterium density (LDD)" [42].

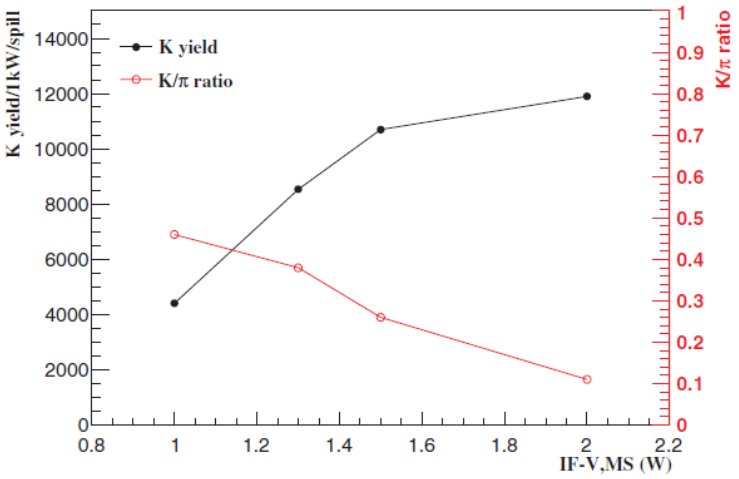

(a) K^- yield and K^-/π ratio

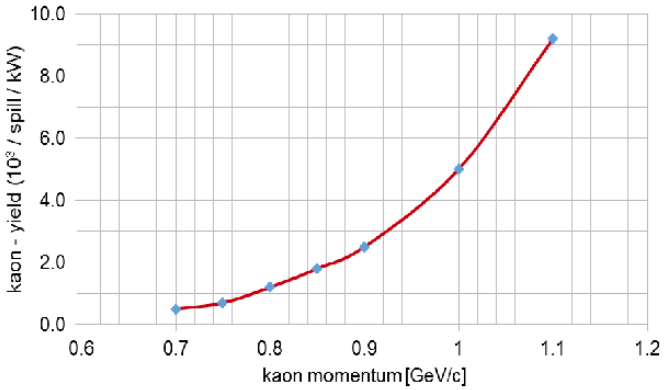

(b) Measured kaon yields at K1.8BR

Figure 4.4: The obtained 1.0GeV/c K^- yield and K^-/π ratio as a function of gap distance between the IF and the MS with an ES1 field of 50 kV/cm is shown.The K^- yield is normalized by a power of 1.0 kW (top).
Measured kaon yields (Run 29 + Run 62) from 0.7 GeV/c to 1.1 GeV/c, normalised to the Run 62 data, recorded in April 2015 (bottom).

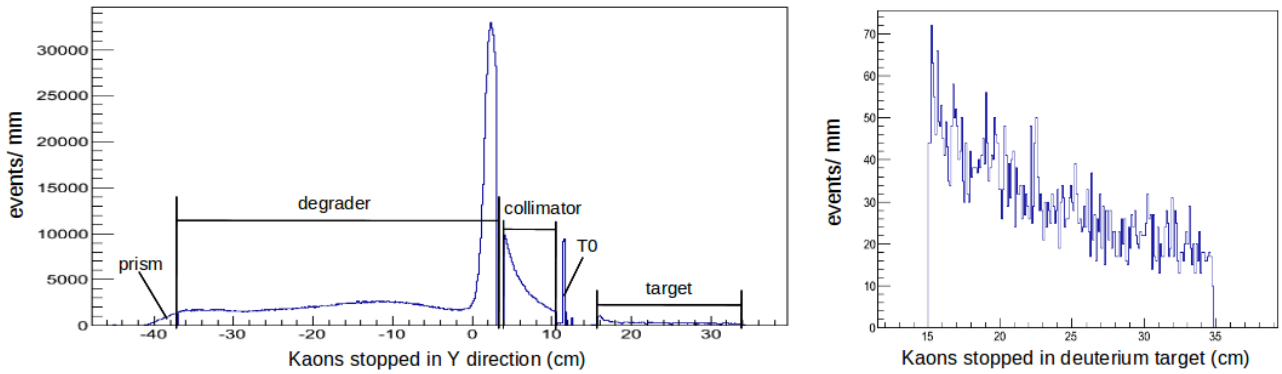

(a) gaseous target with a density of 5% LDD

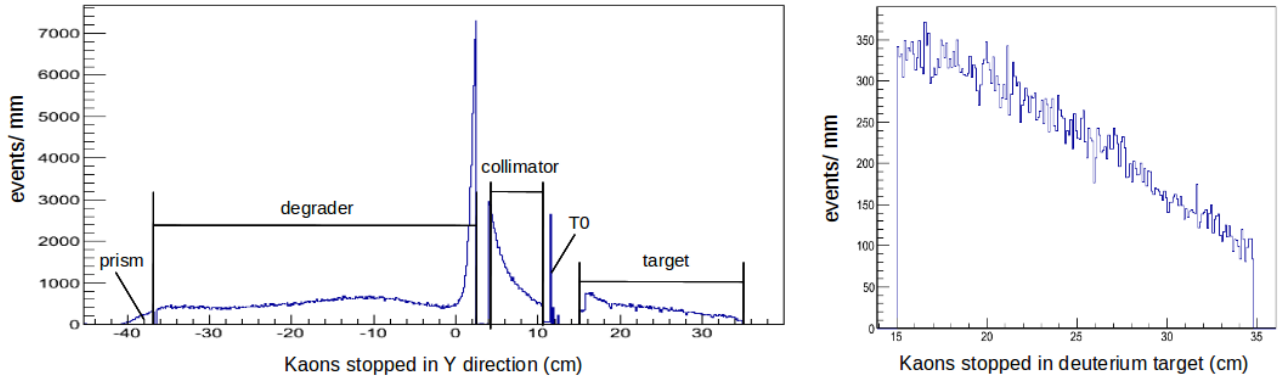

(b) liquid target

Figure 4.5: Kaon stopping distribution from degrader to target (left); kaon stops in the deuterium target(right). An additional prism-shaped degrader of carbon, in front of the main degrader, was used to compensate the position dependence of the momentum. Due to the hight momentum of the kaons a 40 cm degrader is needed in order to stop the particles into the target. As can be seen, 90% of kaons are stopped in the last 4 cm of the degrader and only $0.5{\cdot}10^{-3}$ per beam kaon into 5% (LDD) target. For the liquid case, $9.5{\cdot}10^{-3}$ per beam kaon are stopped into the target.

4.3.2 The trigger effect

In order to measure the X-rays from the kaonic deuterium atoms a two level trigger is applied. The trigger for the E57 experiment will follow the trigger logic of the E17 experiment, for more detail see [40]. The elementary beam trigger is constructed by coincidence signals from the beam line counters, BHD and T0. The kaon beam trigger (K($_{beam}$) is made from the elementary beam trigger by using the kaon identification counter and a veto signal of the Aerogel Cherenkov counter (AC) defines the kaon beam. A logical expression of the kaon beam trigger is given as:

$$(K_{beam}) \equiv (BHD) \otimes (T0) \otimes (\overline{AC}) \tag{4.1}$$

The stopped K^- trigger ($K_{stopped}$) is generated by the signal from E0, DEF and the signal from the veto counter $\overline{BVC}$ with the kaon beam definition:

$$(K_{stopped}) \equiv (K_{beam}) \otimes (E0) \otimes (DEF) \otimes (\overline{BVC}) \tag{4.2}$$

For the first-level trigger, one or more CDH hits (CDH1) are required to reduce the trigger rate and obtain the reaction vertex. A hit in the SDD is required in the second level, because the timing of the SDD signal from the shaping amplifier is too late for the trigger timing of the first level. Therefore the E57 main trigger is:

$$(E57_{1st}) \equiv (K_{stopped}) \otimes (CDH) \tag{4.3}$$

$$(E57_{2nd}) \equiv (E57_{1st}) \otimes (SDD) \tag{4.4}$$

In addition to that, using the vertex cut method with a defined volume inside the target (5 mm away from the walls) and considering the improved timing capability of the new SDD (running the SDD at a temperature below 50 K reduces the drift time to approx. 100 ns), one could clearly see a drastic improvement in the signal to background ratio.

The final numbers are summarised in table 4.3, while figure 4.7 shows the spectrum achieved with a signal-to-noise ratio of 1:4. We calculate for a beam power of 40 kW and 80 % duty cycle that we produce 30 K_α events per day, with the assumptions that K_α events are produced with a yield Y(K_α) of 0.1% and a total active detector area of 246 cm^2 is used. In total, approximately 800 K_α will be collected, which will permit the determination of the shift and width with a precision of 60 eV and 140 eV, respectively. The statistical significance of the K_α-line is approximately 12 σ.

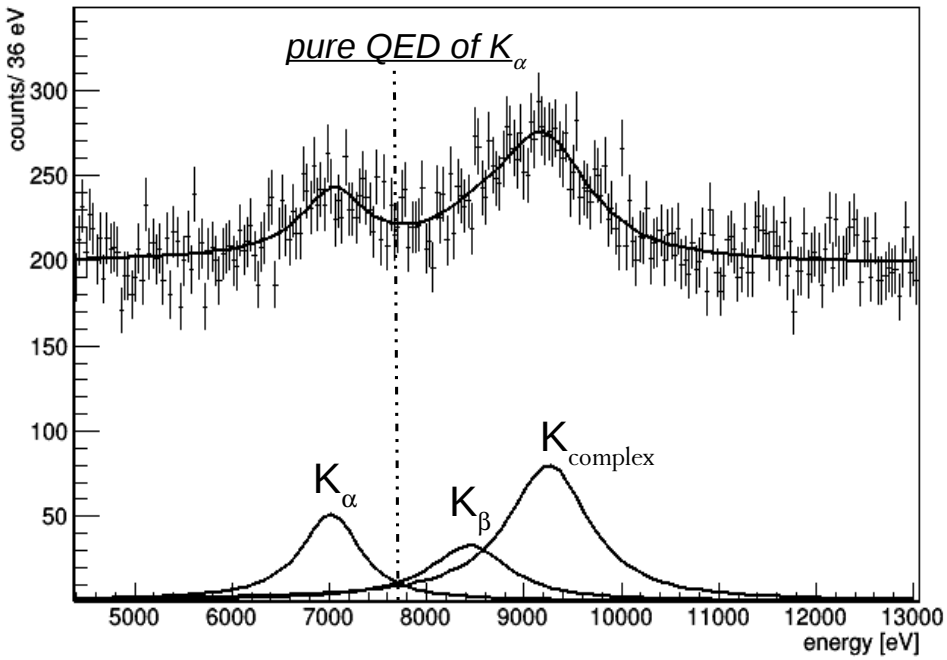

Figure 4.6: Simulated kaonic deuterium spectrum assuming an X-ray yield of 0.1%. Shift is -800 eV and a width 800 eV and . Almost 800 K_α could be collected, which leads to a precision of the fit result in this statistical sample of: 60 eV (shift) and 140 eV (width). The dashed line at 7834 eV shows the pure QED value of K_α.

4.4 Comparison MC and real data

A comparative study of the MC results with the real data taken at the K1.8 BR in June 2016 is presented. The purpose of the beam commissioning was to show good control and understanding of the K^- stopping, to confirm the SDD operation in the real beam condition and to prove the effectiveness of the MC calculation.

For the beam tuning test, the E57 setup was modified removing the magnet, the drift chamber and part of the CDH. While a small chamber (FDC1) placed below the target was used to reconstruct the vertices of the kaons beam and a movable degrader of copper was added in order to optimize the K^- stopping into a 216 cm^3 lithium target with a density of 5 g cm^{-3}. In figure 4.7 a sketch of the setup is shown.

The kaonic Li X-ray yield used for the simulation is 0.15 according to the ref. [43]. Results of the simulation for 0.7 and 0.9 GeV/c kaon momentum are summarize in the first 2 columns of Table 4.4, while the last column refers to the real data (0.9 GeV/c) acquired

Kaon yield at T0 (per spill and kW)	500
$(K_{beam}) \equiv (BHD) \bigotimes (T0) \bigotimes (\overline{AC})$	13
$(E57_{1st}) \equiv (K_{stopped}) \bigotimes (CDH)$	8
stopped kaons in gaseous deuterium	$0.31 \cdot 10^{-3}$
total synchronous BG per keV at 7 keV	$6 \cdot 10^{-2}$
synchronous BG per keV at 7 keV	
with fiducial cut and charged particle veto	$1.5 \cdot 10^{-4}$
asynchronous BG per keV at 7 keV	$1.5 \cdot 10^{-5}$
detected $K_\alpha$events for a yield Y(K_α)=0.1%	
with fiducial cut and charged particle veto	$5 \cdot 10^{-5}$

Table 4.3: Starting point for the evaluation of the background rates and the finally produced K_α events are the number of kaons per spill and kW at the beam counter T0 (taken from E57 Proposal for J-PARC 50 GeV Proton Synchrotron). This kaon number, to start with, is extracted from the E15 measurement in April 2015.

during the test beam. The table shows the kaon beam parameters used for the MC, like number of kaons per spill per kW, kaon momentum, spill length and the results obtained in the simulation. The interesting numbers, for our propose, are the stopping efficiency and the number of detected X-ray/ hour, which are both in accordance with the real data.

	MC 700 MeV/c	MC 900 MeV/c	RD 900 MeV/c
kaon/spill/kW	500	3000	3150
beam power[kW]	40	40	41
kaon/spill	20000	120000	126000
stopping eff.	$7.9 \cdot 10^{-3}$	$1.8 \cdot 10^{-3}$	$1.1 \cdot 10^{-3}$
SDD acceptance	0.033	0.033	0.0265
number of SDD	24	24	24
spill length [s]	6	6	5.52
number of spill /hour	600	600	652.173
X-ray yield	0.15	0.15	0.15
detected X-ray/hour	$1.5 \cdot 10^2$	$2 \cdot 10^2$	$2.4 \cdot 10^2$

Table 4.4: Comparison between MC results for kaon momentum of 0.7 GeV /c and 0.9 GeV /c, respectively first and second column and real data with a beam of 0.9 GeV /c last column.

The experimental results are seen to be in very satisfactory agreement with the MC values. The simulation has confirmed that the background components have negligible effect on the setup, due to the hight efficiency of the trigger system, summarized as follow:

- ID and Trigger efficiency: 0.7

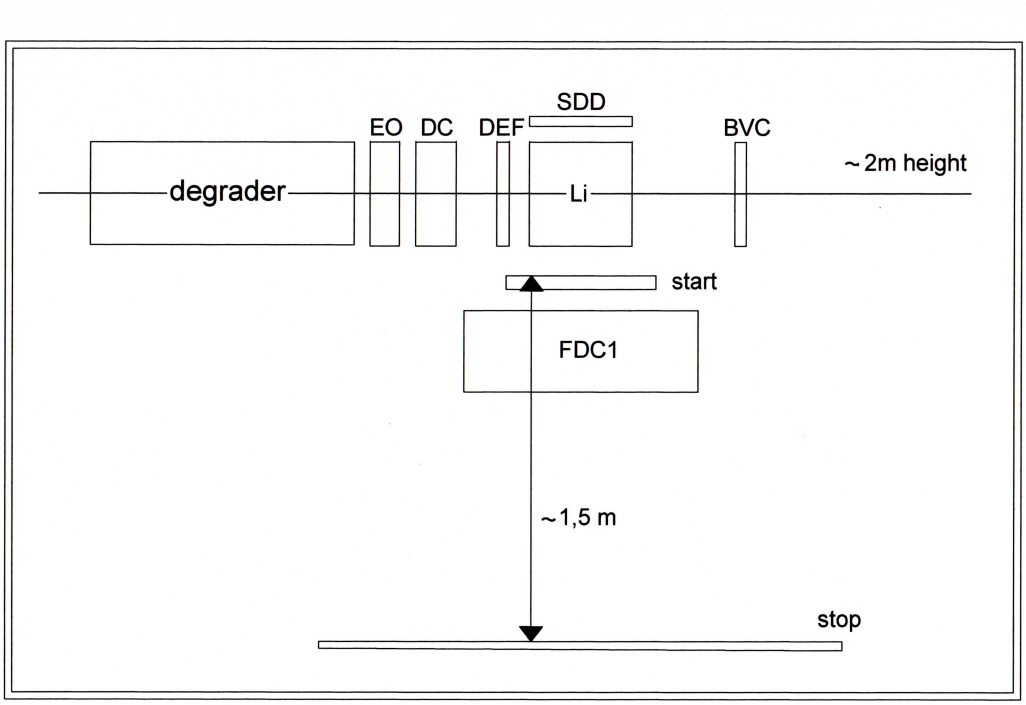

Figure 4.7: beam tuning setup (side view).

- K trigger purity: 0.9
- Acceptance for secondary particles (/stopped K^-): 0.04
- FDC1 efficiency: 0.9

Fig 4.8 and 4.9 show the vertex reconstruction by the FDC1, which was used to apply the fiducial cut, while in Fig 4.11 the energy deposit on E0 counter shows as a clear correlation was observed for both K^- and K^+ beam.

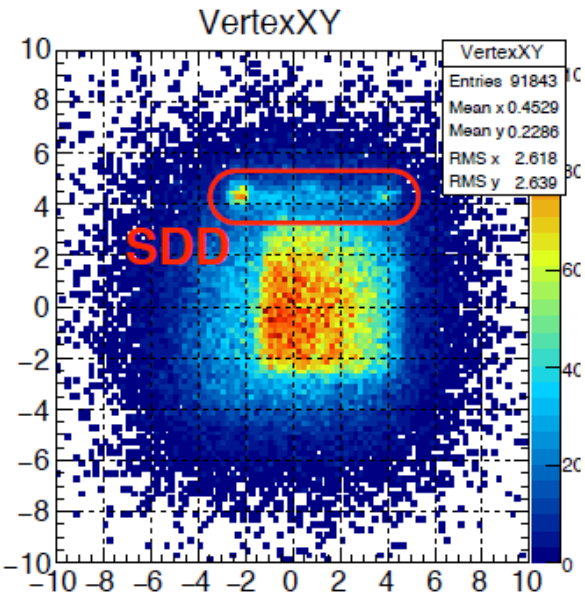

Figure 4.8: Event vertex with the kaon beam reconstructed by the FDC1. The cross sections of perpendicular directions to the beam axis is show.

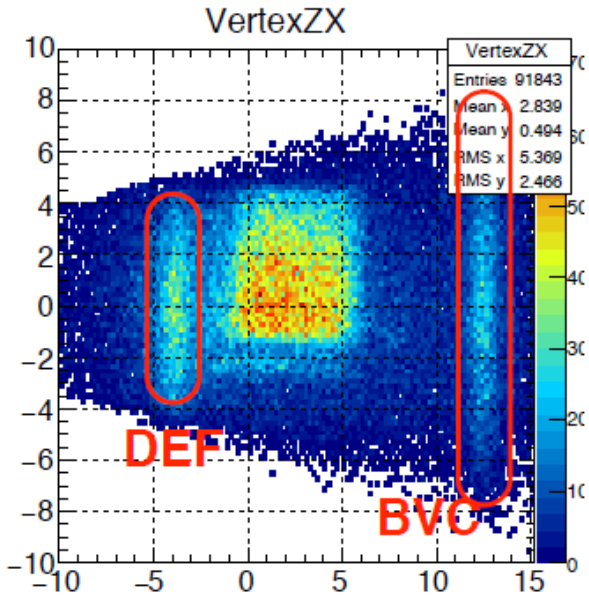

Figure 4.9: Event vertex with the kaon beam reconstructed by the FDC1. The cross sections of parallel directions to the beam axis is show.

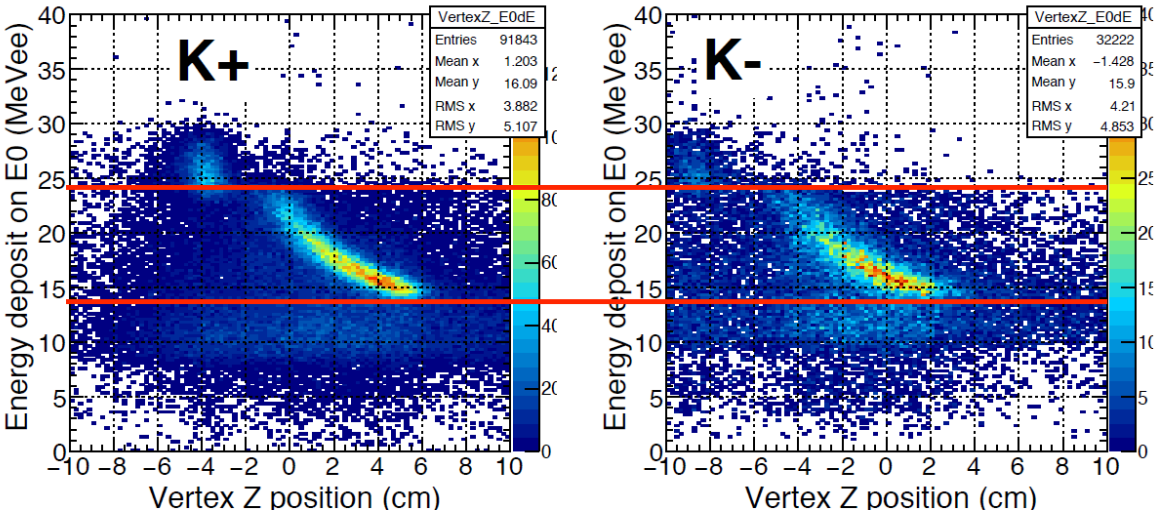

Figure 4.10: energy deposit on E0 counter by K^- and K^+ beam depending on vertex position.

5 X-ray detector

To perform a high-precision X-ray spectroscopic measurement of the exotic system two fundamental characteristics of the spectrometer are needed. The first is a good energy resolution and a low intrinsic noise, the second is a high-rate capability. In this chapter, the working principle and main characteristics of the SDD devices are given. Experimental tests and characterizations of the devices are also presented in the last section.

5.1 The SDD working principles

The basic form of the Silicon Drift Detector (SDD) was proposed in 1983 by Gatti and Rehak [44]. “It consist of a radial electric field which is intentionally established and controlled by a number of increasingly reverse-biased circular field strips covering one surface of the device. This field terminates in a very small collecting anode on one face of the device. The design of an example SDD, Figure 5.1 (a), demonstrates this ring electrode structure, which creates the radial electric field. The radiation entrance window on the opposite side is composed of a thin, shallow implanted p+ doped region, which provides a homogeneous sensitivity over the whole detector area" [45], called Back. On the other side the p+ contacts are shaped as concentric rings, placed around the n+ anode ring. The SDD is fully depleted, biasing with a negative voltage the p+ contacts, leaving only a small undepleted region near the anode . The negative charge carriers produced in the detection phase, are collected at the n+ anode thanks to an electric field properly shaped as a conveyor, whilst the positive charge carriers are captured by the nearest p+ contact. The shaping of the electric field is obtained by applying progressive negative voltages to the rings. The outermost ring corresponds to the lower voltage (-156 V), while on the first ring the highest voltage (-25 V) is applied. The electric field shape is shown in fig. 5.1 (b). If the minimum of the potential falls slightly out the position of the anode, an effect which can be due to the structural characteristics of the SDD or to incorrect working conditions set, we can have incomplete charge collection effects which must be taken into account in the study of the response function of the spectrometer. The particular geometry

of the SDDs allows to enlarge the active area and to minimize at the same time the anode capacitance.

A PN-diode is depleted biasing with a positive voltage the anode n+, therefore to obtain a large active area is required a large area anode, which enhance the anode capacitance. On the contrary, in a SDD detector, the dimensions of the active area are not depend on the anode dimensions, thanks to the lateral depletion technique and the drift field to collect the charge on the anode. It is therefore possible to minimize the anode and consequently the anode capacitance. The reduced anode capacity gives rise to higher output signals, which means that events with lower charge collection can be acquired; it also implies a reduced Equivalent Noise Charge (ECN). The ENC is defined as a signal that would create a signal over background (S/B) exactly equal to 1. As a consequence of these characteristics, charge collection times are in the range 250 ns - 1 μs (depending on the detector surface) and rates bigger than 10^5 Hz can be reached, allowing also the use of an external trigger.

5.1.1 The intrinsic noise and response function of the SDD

In a good approximation, SDD response function is a gaussian curve as in every silicon detector; the width of the peak is a fundamental parameter for our analysis. This parameter is related to the Fano factor, to the electron-hole pair creation energy and to the intrinsic noise factors. The relationship between the FWHM, σ and these parameters is:

$$\sigma = \frac{FWHM}{2.35} = \omega\sqrt{W_N^2 + \frac{F \times E}{\omega}} \tag{5.1}$$

being ω the e-h pair creation energy (3.81 eV), F the Fano factor ($\simeq 0.1$), E the energy of the line and W_N^2 the intrinsic noise of the detector. While ω parameter is constant in our experimental condition, the other two parameters are strictly dependent on temperature and on construction procedure of the Si wafer and have to be determined for each single detector during the fitting procedure.

The intrinsic noise of the SDDs is related to statistical fluctuations of the number of carriers generated by an ionizing particle and it depends only on the the materials which the detector is made of. For an incident photon with E energy, the average carriers' number is

$$\overline{N} = \frac{E}{\omega} \tag{5.2}$$

ω value depends on the materials. The e-h pair creation process is not strictly poissonian being non totally independent by the creation of other e-h pairs. Fano factor, together

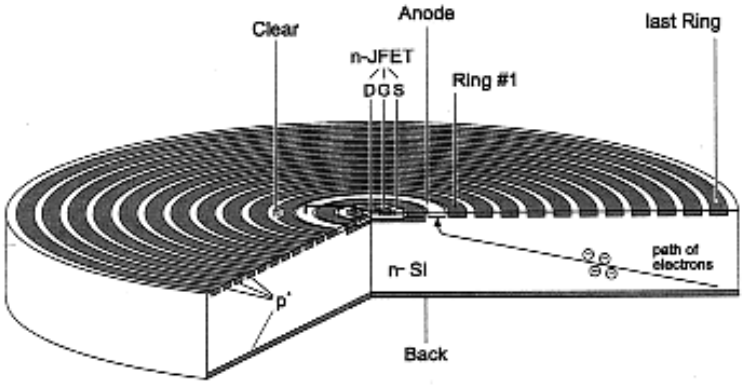

(a) SDD structure with integrated JFET preamplifier.

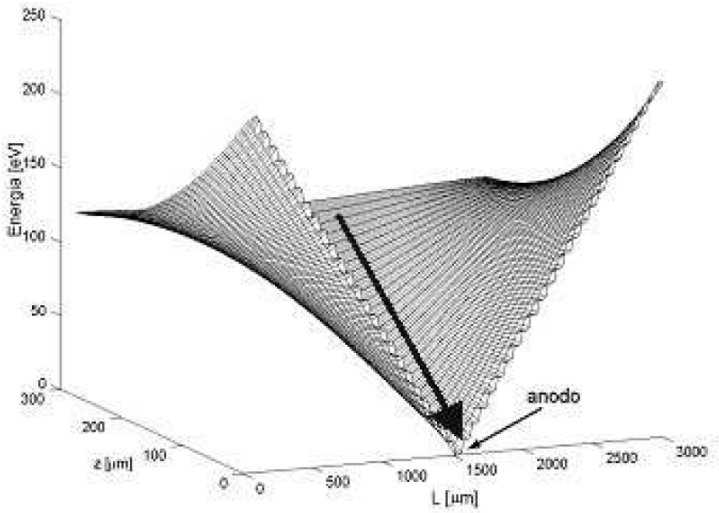

(b) Potential inside the SDD generated by an electric field parallel to the surface.

Figure 5.1: The schematic drawing of the Silicon Drift Detector (top). The SDD drift field, properly shaped as a conveyor (bottom) [46].

with the e-h creation energy factor, is a crucial parameter that influences the resolution of the silicon detector. Eventually the noise becomes small enough that resolution becomes almost entirely limited by Fano broadening. Fano broadening is based on statistical fluctuations in the radiation interaction with the Si crystal lattice and the charge production process. When this limit is reached, the theoretical best resolution is roughly 120 eV.

5.1.2 Fine structure of silicon detectors response

The actual spectral response of Si detectors is predominantly gaussian, but has a low energy component whose relative intensity depends upon the fabrication process, incomplete charge collection and electrons escape, and a high energy tail due to pile-up effect. While the pile-up effect is essentially a gaussian shifted to higher energy with respect to the main peak, the low energy component is a bit more complicated, but it can be accurately modelled and studied [47–51]. Three main components have to be taken in account:

- In a real detector the sharp line (delta function) that a photon would produce is broadened by electronic noise into a Gaussian shape
- An effect of incomplete charge collection that could remove counts from the main peak [47] producing, in an ideal detector, an exponentially decaying distribution below the peak that for real detector has to be broadened
- An invariably observed flat shelf running from the main peak down to very low energy

The final shape of the peak is then the convolution of the three components: gaussian (G), exponential decay (E) and shelf (S)

$$G(x) = H_G e^{\frac{-(x-x_0)^2}{2\sigma^2}} \tag{5.3}$$

$$E(x) = H_D e^{\frac{x-x_0}{\beta}} \qquad x < x_0 \tag{5.4}$$

$$E(x) = 0 \qquad x \geq 0 \tag{5.5}$$

$$S(x) = \frac{1}{2} H_D e^{\frac{x-x_0}{\beta}} e^{\frac{\sigma^2}{2\beta^2}} \cdot erfc\left(\frac{x-x_0}{\sigma\sqrt{2} + \frac{\sigma}{\beta\sqrt{2}}}\right) \tag{5.6}$$

being H_G the height of the Gaussian, H_D the height of the exponential at the Gaussian centroid, β the slope of the exponential and *erfc* the complementary error function.

5.2 SDDs characterization during the E-57 test beam

5.2.1 The SDD setup

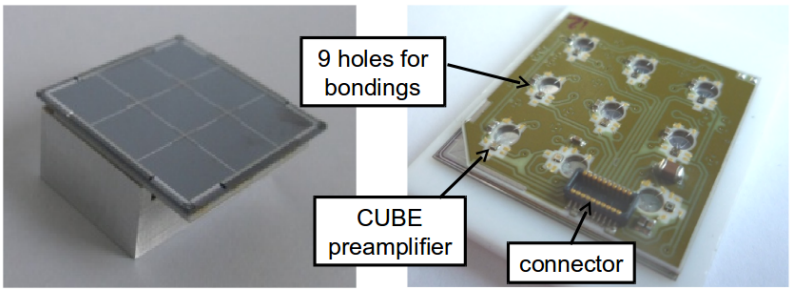

Figure 5.2: 3x3 matrix. Frontside (left); backside (right).

The SDDs were organized in 4 monolihic arrays of 9 elements (0.8 cm x 0.8 cm each, total area 23 cm^2) in a 3x3 format. The array is mounted on a ceramic carrier and a copper block is connected below the board in order to cool the detector. The read-out of the SDDs is based on a CMOS preamplifier (CUBE) recently developed at Politecnico di Milano. This circuit provides similar or even better performances in terms of electronics noise with respect to the more conventional JFET readout, in particular at short shaping times.

CMOS technology is intrinsically more robust at lower temperatures than the more conventional JFET transistor used in SDDs readout and it allows the use of these devices at much lower temperatures. “At lower temperatures the drift time of the charge in the SDD is reduced due to the increase of the electron mobility in the silicon. The effect is the reduction of the ballistic deficit and the reduction of the tail in the spectra with a consequent improvement in the resolution" [41]. Short drift time is important for the timing of the experiment in order to reject the high background.

At lower temperatures also the leakage current decreases. Leakage current which results from the bias voltage applied to the sensor, gives rise to the slope on the voltage ramp. Leakage current is a source of “shot noise” and affects resolution at long process times where the base-line signal changes over the time taken to integrate the ramp. For a given design of detector, leakage is proportional to the area and thickness of the sensor and increases with increased temperature. To achieve best resolution, SDD detectors require long process times to reduce voltage noise and therefore require extensive cooling to minimise leakage current noise.

For this characterization the SDD has been cooled with 3 stage Peltier elements to a minimum temperature of -50 C (average -40 C). The peltier holder was water cooled (max. 7 bar water overpressure). Two temperature sensors (LakeShore Pt-100) were mounted on copper block and on the cold finger in order to control the SDDs temperatures.

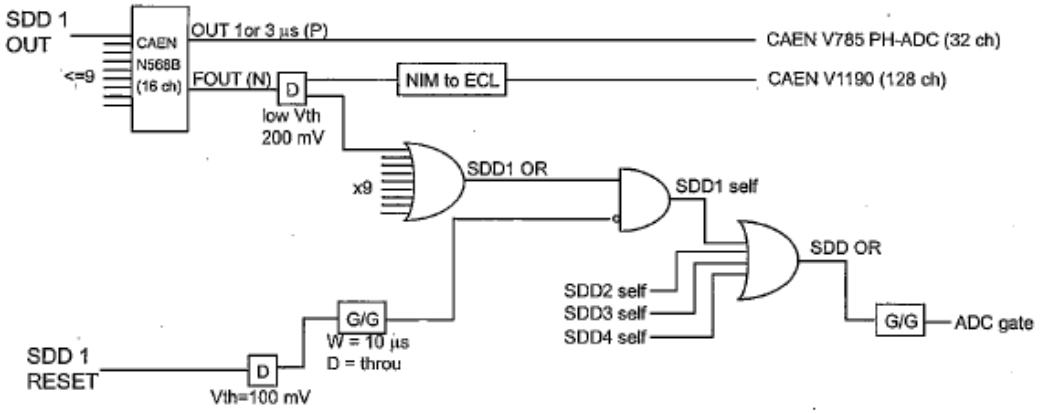

Figure 5.3: DAQ logic. Only the SDD unit 1 layout is shown completed as an example, the other 3 units follow the same logic.

Each array has its own preamplifier board. In this configuration, the analog output of the CUBE and preamplifier for each SDD element goes through the following chain. First is fed to the CAEN N568B spectroscopic shaping amplifier. The Gaussian shaped analog output with 3 μs shaping time goes to the CAEN V785 ADC, which digitises the height of the Gaussian pulse. The N568B amplifier has also a fast output (Fout) with a rise time of 25 ns. This signal fed into a discriminator and used for the trigger logic. As shown in Fig. 5.3, the ADC gate is defined by the OR logic of all the SDDs when there is no RESET from the SDD chips arriving. Furthermore, the digitised Fout signal are logged by the CAEN. V1190 TDC, where the time difference from the kaon beam for each SDD element is recorded as SDD timing for the selection of kaon-origin events.

5.2.2 The calibration procedure

This section describes the calibration procedures of all the production spectra, acquired in the data-taking period. In an high precision X-ray spectroscopic measurement the quality of the calibration procedures plays a fundamental role in extracting the final result; the response of each SDD detector must be carefully studied and checked for all the data-taking periods, to evaluate the systematic errors. In order to achieve good analysis results, an accurate selection of the detectors has to be done before the test beam using a ^{55}Fe source. We have selected 24 good SDD-channels over 36. Fig. 5.4 reports the spectrum of the

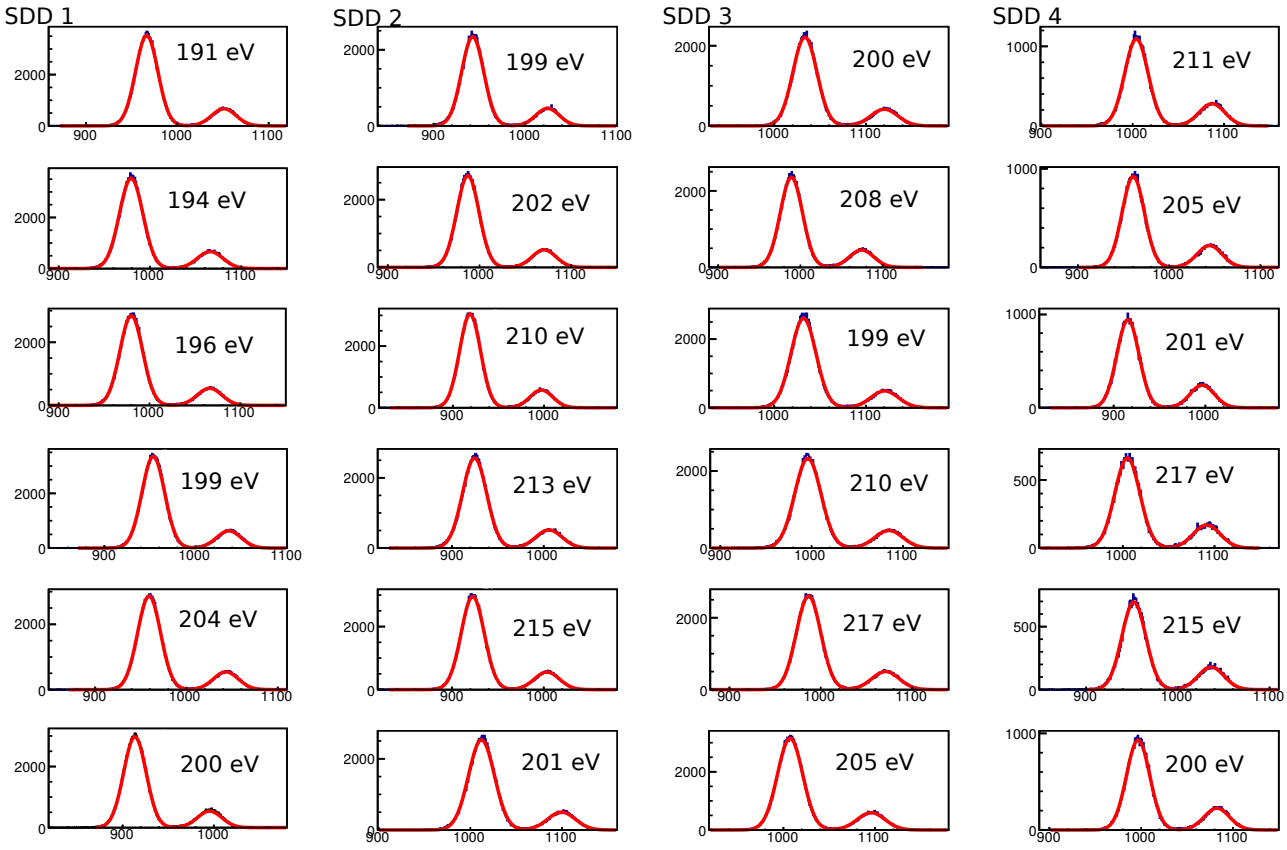

Figure 5.4: Spectra of all the 24 channels acquired in a parallel acquisition. The energy resolution of the Mn-K_α-line of the ^{55}Fe calibration source is shown. Each column correspond to a single SDD array. The differences between channels are due to the different leakage currents.

Mn-K_α-line of the ^{55}Fe source at 3μs shaping time with a measured energy resolution of $\sim$ 200 eV. Finally as a main calibration source we use ^{57}Co which is suitable in our case since the γ ray (14.41 KeV) is close to the kaonic lithium line. The source was placed close to the detector during the data taking, under beam-on operation and beam-off condition. The ^{57}Co source provides Fe K-series lines and the γ_1 transition of Co. The reference energies of these calibration sources are listed in Table 5.1. The calibration is performed for each detector and main steps are:

- Initially an automatic search of the peak position starts in order to have initial parameters to insert in the main fitting procedure
- Main fitting procedure is done with MINUIT [root], and is performed calling MIGRAD and MINOS functions.
- Energy difference between K_α, K_β and γ_1 lines are fixed according to table 5.1.

- σ of each peak is defined according to eq. 5.1; one of the three parameters has to be fixed in order to obtain meaningful results and the choice is to set ω (e-h pair creation energy) fixed since it's the least energy and temperature dependent and can be considered common for all SDDs. Value is taken from literature [52] and is ω = 3.81 eV.
- Background is set to be a linear polynomial function.

Nuclide	Half-life	Type of decay	Photon Energy Emission (Mev)	prob.
^{55}Fe	2.73 y	EC	Mn K x rays:	
			0.00590	24.4%
			0.00649	2.86%
^{57}Co	0.744 y	EC	0.014	9%
			0.122	86%
			0.136	11%
			Fe K x rays	58%
			0.0064	33.6%
			0.00706	3.9%

Table 5.1: Calibrations sources used during the E57 test beam. Revised November 1993 by E. Browne (LBNL).

In the case of the Li data, calibration spectra were accumulated using a ^{57}Co source at intervals during all runs (see run summary, Fig.5.8). Two examples of typical calibration spectra obtained with and without kaon beam are shown in fig. 5.6, the detector for both cases SDD number 1 first cell is used. The energy to ADC channel correspondence was determined using the peak position of the Fe K_α and $Co_{\gamma 1}$. The conversion factor (slope) is obtained from

$$slope = \frac{^{57}Co\gamma_1(ch) - FeK_\alpha(ch)}{^{57}Co\gamma_1(eV) - FeK_\alpha(eV)} \tag{5.7}$$

The energy resolution of this channel was 268 eV (FWHM) at 14.41 keV and 205 eV (FWHM) at 6.4 KeV during calibration and K run. Due to the similar energies of $Co_{\gamma 1}$ and the $K^-Li_{L\alpha}$ transition, the choice of this calibration give us a good linearity close to the energy region of Kaonic lithium. Fit results of SDD 1 channel 1 are shown in Tab. 5.2.

5.2.3 Stability studies

E57 took data with different beam momentum, trigger condition and degrader length. Data are divided in various sets and summarized in Fig. 5.8. We used 0.9 GeV/c K^+, K^- and

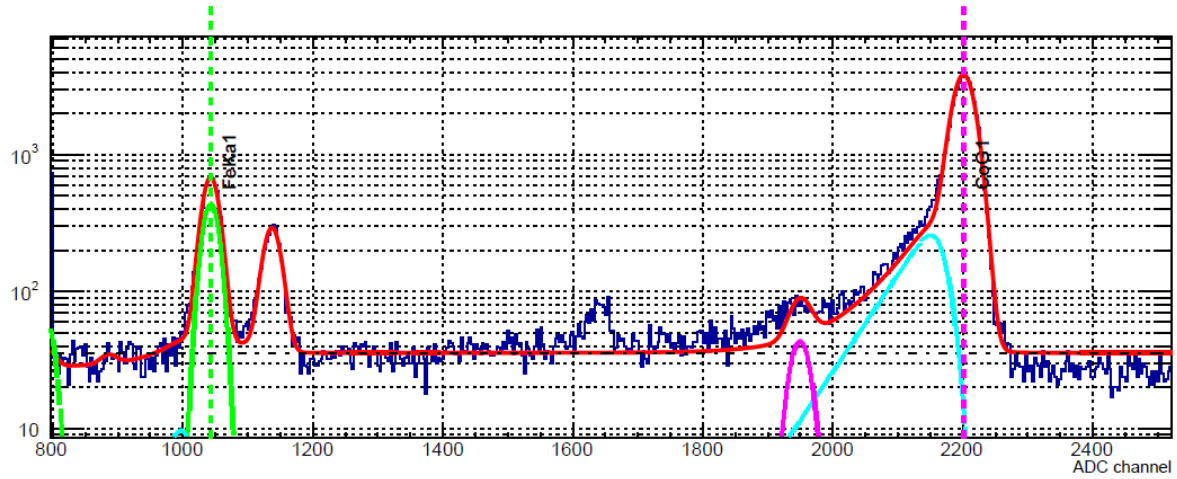

(a) kaon beam off

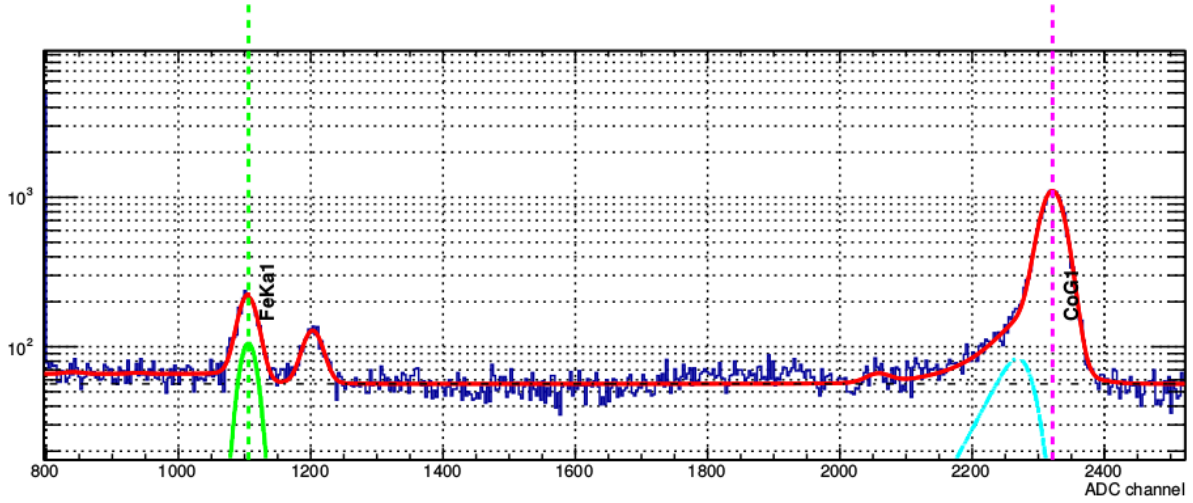

(b) kaon beam on

Figure 5.5: Typical calibration spectra obtained with and without kaon beam.

parameter	value	error
P0	$1.16986 \cdot 10^{2}$	$3.355 \cdot 10^{-1}$
P1	$1.44615 \cdot 10^{2}$	$2.529 \cdot 10^{-5}$
slope	0.144615	$2.529 \cdot 10^{-5}$
ω	3.81	
Fano factor	0.18027	$7.063 \cdot 10^{-3}$
Constant noise	7.5057	0.5198
$^{57}Co_{\gamma 1}$ peak events	$6.1 \cdot 10^{4}$	$5.8 \cdot 10^{2}$
$^{57}Co_{\gamma 1}$ tail events	$2.48 \cdot 10^{4}$	$1.6 \cdot 10^{2}$
$Fe_{K\alpha}$ peak events	$2.05 \cdot 10^{4}$	$1.7 \cdot 10^{2}$
$Fe_{K\alpha}$ tail events	$7.12 \cdot 10^{2}$	$2.6 \cdot 10^{1}$
escape	$1.062 \cdot 10^{-2}$	$8.220 \cdot 10^{-4}$

Table 5.2: Example of a fit results for calibration without kaon beam (SDD 1 ch 1). P0 and P1 are the linear background parameters, ω is the e-h pair creation factor, while slope is the conversion factor (ch/eV).

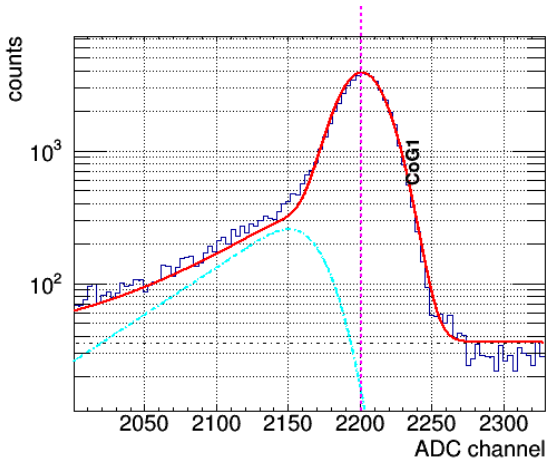

Figure 5.6: ^{57}Co fit. Only Gauss and Tail were used for the fitting.

0.7 GeV/c K^+, K^- kaon-tuned beams. Various conditions in terms of hit rates on the Defining counter were realized by changing the IF-V slit width. We obtained the data with diverse hit rates depending on trigger condition and beam momentum. Studies of response function in various conditions are crucial for the suppression of the systematic error, all runs were taken in to account, depending on the rate, beam condition and trigger. For the stability studies, only the ^{57}Co peak was used because the statistic of the Fe peak was too low in most runs.

The change in the position of the 14.41 keV peak over the period of the whole run was found to be $\sim$ 10 eV (see Fig. 5.7 bottom), while, if we consider only the calibrations runs (see Fig. 5.7 top), the changes in the position is less then 4 eV. The reason for the

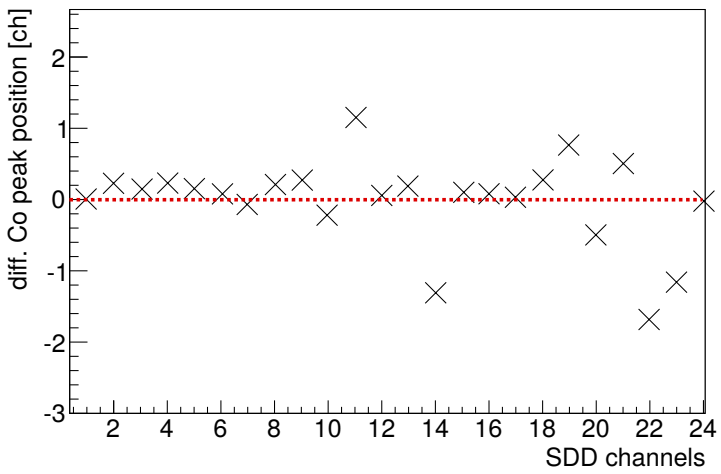

(a) Shift of the ^{57}Co between two different calibration run.

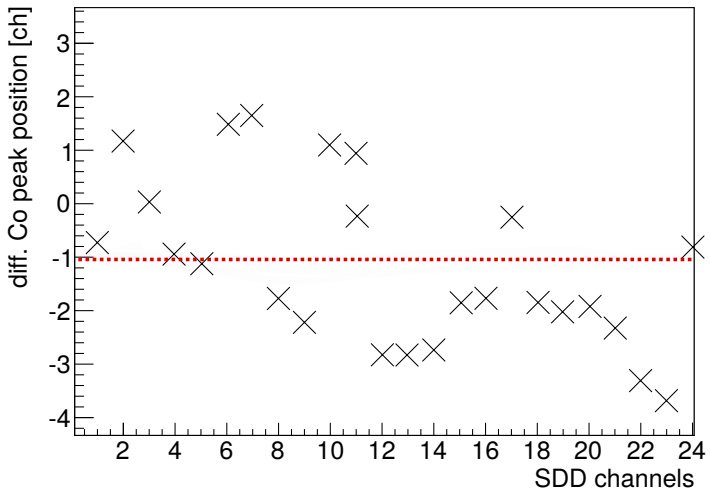

(b) Shift of the ^{57}Co between calibration and kaon run.

Figure 5.7: Stability of the ^{57}Co peak position.

discrepancy in the graph is due to the high background rate during kaon beam, which is confirmed by the negative shift on the second plot.

Run	beam	57Co	WSD	deg	start	stop	spils	trig
508	-0.9	IN	IN	20	16:01	16:53	564	
509	-0.9	IN	IN	20	16:53	17:07	652	
510	-0.9	IN	IN	15	17:09	17:16	77	Kstop|| SDD_SPILLOFF
511	-0.9	IN	IN	15	17:17	17:22	39	pi
512	-0.9	IN	IN	15	17:22	17:59	402	Kstop
513	-	IN	-	-	23:36	00:37		self
514	check run							
515	check run							
516	-0.9	IN	IN	15	9:24	10:23	639	Kstop||SELF_SPILLOFF
517	-0.9	IN	IN	20	10:26	11:25	639	Kstop||SELF_SPILLOFF
518	-0.9	IN	IN	25	11:26	12:25	633	Kstop||SELF_SPILLOFF
519	-0.9	IN	IN	30	12:27	12:46	198	Kstop||SELF_SPILLOFF
520	-0.9	IN	IN	27	12:47	13:42	579	Kstop||SELF_SPILLOFF
521	-0.9	IN	IN	15	13:47	14:45	638	Kstop||SELF_SPILLOFF
522	-0.9	IN	IN	10	14:47	15:41	588	Kstop||SELF_SPILLOFF
523	-0.9	IN	IN	17	16:35	17:29	588	Kstop||SELF_SPILLOFF
524	-0.9	IN	IN	23	17:32	18:33	645	Kstop||SELF_SPILLOFF
525	-0.9	IN	IN	23	18:33	18:34		pi trigger
526	-	IN	-	-	18:34			
527	-0.9	OUT	IN	20	8:36	8:39	30	pi
528	-0.9	OUT	IN	20	8:42	8:45	37	Kstop||SELF_SPILLOFF
529	-0.9	OUT	IN	20	9:00	10:05	691	Kstop||SELF_SPILLOFF
530	-0.9	OUT	IN	20	10:08	11:09	653	Kstop||SELF_SPILLOFF
531	-0.9	OUT	OUT	30	11:34	12:38	684	Kstop||SELF_SPILLOFF
532	-0.9	OUT	OUT	37	12:41	13:43	681	Kstop||SELF_SPILLOFF
533	-0.9	OUT	OUT	15	13:45	14:05	215	Kstop||SELF_SPILLOFF
534	-0.9	OUT	OUT	23	14:06	15:08	677	Kstop||SELF_SPILLOFF
535	-0.9	OUT	OUT	27	15:10	16:09	610	Kstop||SELF_SPILLOFF
536	-0.9	OUT	OUT	27	16:11	16:28		Kstop||SELF_SPILLOFF
537	-0.9	OUT	OUT	27	16:30	17:27		Kstop||SELF_SPILLOFF
538	-0.9	OUT	OUT	27	17:29	18:17		Kstop||SELF_SPILLOFF
539	-	IN	-	-	21:26	22:03		SELF
540	-	IN	-	-	22:09	08:30		SELF
541	-	IN	-	-	12:43	14:45		SELF
542	+0.7	IN	OUT	15	14:57	15:14		(SELFxONSPILL)
543	+0.7	IN	OUT	10	15:14	15:29		(SELFxONSPILL)
544	+0.7	IN	OUT	20	15:30	15:49		(SELFxOFFSPILL)
545	+0.7	IN	IN	10	15:30	15:50		(SELFxONSPILL)
546	+0.7	IN	IN	5	16:15	16:30		(SELFxONSPILL)
547	+0.7	IN	IN	15	16:37	16:30		(SELFxONSPILL)
548	check run							
549	-0.7	OUT	OUT	15	17:11	18:06	586	KSTOP||(SELFxOFFSPILL)
550	-0.7	OUT	IN	10	18:14	19:13	638	KSTOP||(SELFxOFFSPILL)
551	-0.7	OUT	IN	15(Cu)	19:15	19:22	79	KSTOP||(SELFxOFFSPILL)
552	-0.7	OUT	IN	13(Cu)	19:24	20:10	496	KSTOP||(SELFxOFFSPILL)
553	-0.7	OUT	IN	7(Cu)	20:15	20:56	448	KSTOP||(SELFxOFFSPILL)
554	-0.7	OUT	IN	7(Cu)	20:57	21:00	43	PI
555	-	IN	-	22:32	9:15		SELF	
556	+0.9	IN	IN	50(C)	9:42	10:03		(SELFxONSPILL)
557	+0.9	IN	IN	10(C)	10:04	10:12		(SELFxONSPILL)
558	+0.9	IN	IN	90(C)	10:15	10:19		(SELFxONSPILL)
559	+0.9	IN	IN	70(C)	10:20	10:30		(SELFxONSPILL)
560	+0.9	IN	IN	30(C)	10:31	10:41		(SELFxONSPILL)
561	check run							
562	-0.9	OUT	IN	50(C)	10:58	11:58	635	KSTOP||(SELFxOFFSPILL)
563	-0.9	OUT	IN	70(C)	11:59	12:59	640	KSTOP||(SELFxOFFSPILL)
564	-0.9	OUT	IN	30(C)	13:00	14:01	666	KSTOP||(SELFxOFFSPILL)
565	-0.9	OUT	IN	40(C)	14:03	15:00	621	KSTOP||(SELFxOFFSPILL)

Figure 5.8: Run summary.

6 Kaonic Lithium measurement at J-PARC

In this chapter the kaonic lithium data analysis is presented and discussed. The chapter is organized in three main parts. The first one describes the kaonic Lithium existing experimental results. The second part presents the definition and the optimization of the cut criteria used in the analysis to enhance the Signal over Background ratio. The last part is dedicated to the analysis technique purposely developed for this work and its result.

6.1 The first KLi experimental result

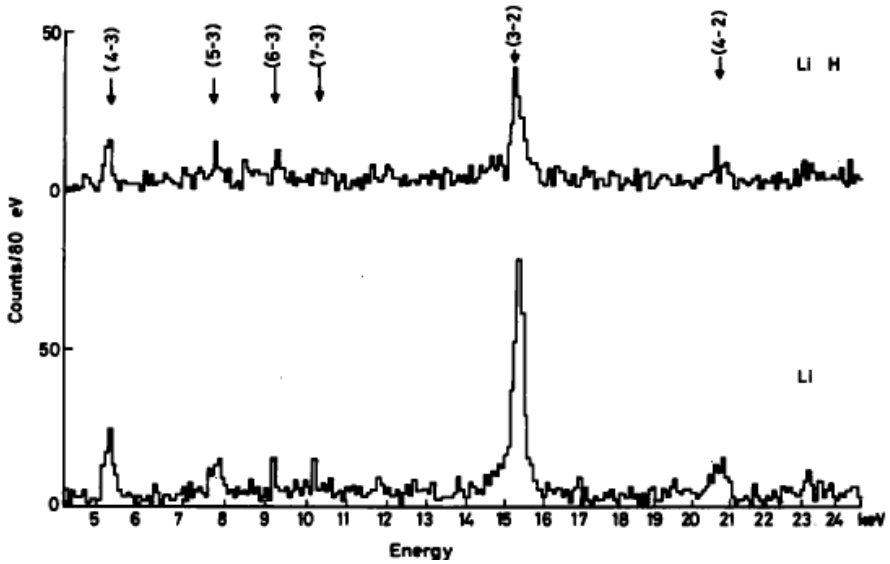

Figure 6.1: Measured spectra obtained with Li (metal) and LiH target. The Li spectra was obtained with $2.7 \cdot 10^7$ kaons stopping in the target whilst for LiH the number of stopping kaons was $1.9 \cdot 10^7$ [53].

The first experiment on K^-Li was performed at Rutherford Laboratory, UK, in 1974 by C. J. Batty et al. They have observed X-rays from kaons stopping in targets of Li, LiH and

Be. They have measured, in the case of the Li, the strong interaction widths and shift of the $3d \rightarrow 2p$ transition. The obtained spectrum is shown in Figure 6.1.

Their experimentally measured energies and calculated electromagnetic transition energies are respectively 15.321 $\pm$0.024 and 15.319 [53]. While the measured shifts and widths is given in table 6.1. We have used Batty's work for comparison with our analysis, since its measurements of the shift and width of the 2p level in kaonic lithium are the only published so far.

Nucleus	(n,l)	Γ_{exp}(KeV)	Γ_{calc}(KeV)	$-\Delta E_{exp}$(KeV)	$-\Delta E_{calc}$ (KeV)
Li	(2,1)	0.055$\pm$ 0.029	0.045	- 0.002 $\pm$ 0.026	0.008

Table 6.1: Strong interaction widths and shifts of K^-Li [53].

6.2 The kaons selection

The kaonic lithium measurement was obtained during the E57 test beam in the period May-June 2016 at the K1.8BR spectrometer at J-PARC. A detailed description of the K1.8BR beam line has already been given in chapter 3, while the setup for the kaonic Lithium measurement is shown in Fig 4.8.

For this measurement, the $K^-Li_{L\alpha}$ transition were detected with 15.4 cm^2 area SDDs, the silicon detectors were placed on top of a 216 cm^3 lithium target. For the calibration we have used a ^{57}Co source at intervals during the data taken. Kaons are discriminated from pions using timing information; we have used T0 and BHD scintillators, which included time-of-flight (TOF) selection, to remove the pions contamination.

An Aereogel Cerenkov counter and two small drift chambers, both upstream and downstream of the degrader, were additionally used to track and reject pions online, while an energy measurement counter E0 is used to reduce the continuum background events.

This section describes the analysis of all the production spectra, acquired in the data-taking period considered. After applying the common cut conditions, summed up spectra of 24 SDDs were studied. In Fig. 6.5 the effects of each single analysis cut is shown.

The architecture of the Data Acquisition system allows to register all the SDD events, both the ones detected in coincidence with the kaon beam and the ones not in coincidence with the beam detectors. The trigger logic for the kaonic lithium measurement (E57$_{K^-Li}$) is defined as:

$$Kaon_{stop} = BHD \otimes T0 \otimes \overline{AC} \otimes E0 \otimes DEF \tag{6.1}$$

$$E57_{K^-Li} = SDD_{self}(SDDOR) \otimes Kaon_{stop} \tag{6.2}$$

SDDOR follows the DAQ logic described in Fig. 5.3. SDD_{self} gives a spectrum without any trigger cut or selection, but simply an all events stored spectrum when there is no RESET from the SDD chips arriving. Each SDD preamplifier operates in a pulsed reset regime periodically resetting the charge accumulated on the feedback capacitance when the output voltage overcomes a given threshold.

The reset time covers the dead time of the preamplifier to recover normal operations and is less than $\sim 1\mu$s [41]. We have applied the RESET veto cut in offline analysis since in the readout electronics the reset pulse introduces noise to the output of the SDD that may have the pulse height similar to the x-ray events of our interest.

The time difference from the kaon beam for each SDD element is recorded as SDD timing for the selection of kaon-origin events. The Drift-Time value is the time difference between a coincidence detected by the T0 counter and the complete charge collection in the SDD which registered a hit.

The time window using for the kaons selection is 8μs. As an example, the distribution for the Drift-Time values is shown in fig. 6.2.

Thereafter, we additionally applied a correlation cut using the E0 detector. The energy measurement counter E0 provides the energy deposited information, used for particle identification, thus we are able to eliminate the background produced in the setup region, as well as the fraction of electromagnetic background collected during their corresponding triggers.

The output pulse of E0 whose width is proportional to time-over-threshold (ToT), is used to extract the energy loss in E0 measuring the pulse width by the leading and trailing edge. In Fig. 6.3 the correlations between the two segmented counters (E0[0] and E0[1]) and the time window cut, Δt = 4.5 ns, for E0[1] is shown.

Kaons were identified using T0 and BHD which included time-of-flight (TOF) selection. TOF resolution between the BHD and T0 is 160 ps. As the Fig. 6.4 shows, the time of flight for kaon and pion has a 5.2 ns peak-to-peak separation, and a range of 2 ns was chosen as optimum for the kaon selection (fig. 6.4 (b)). The optimization of the TOF coincidences windows between BHD and T0 detectors is done according to the following procedure.

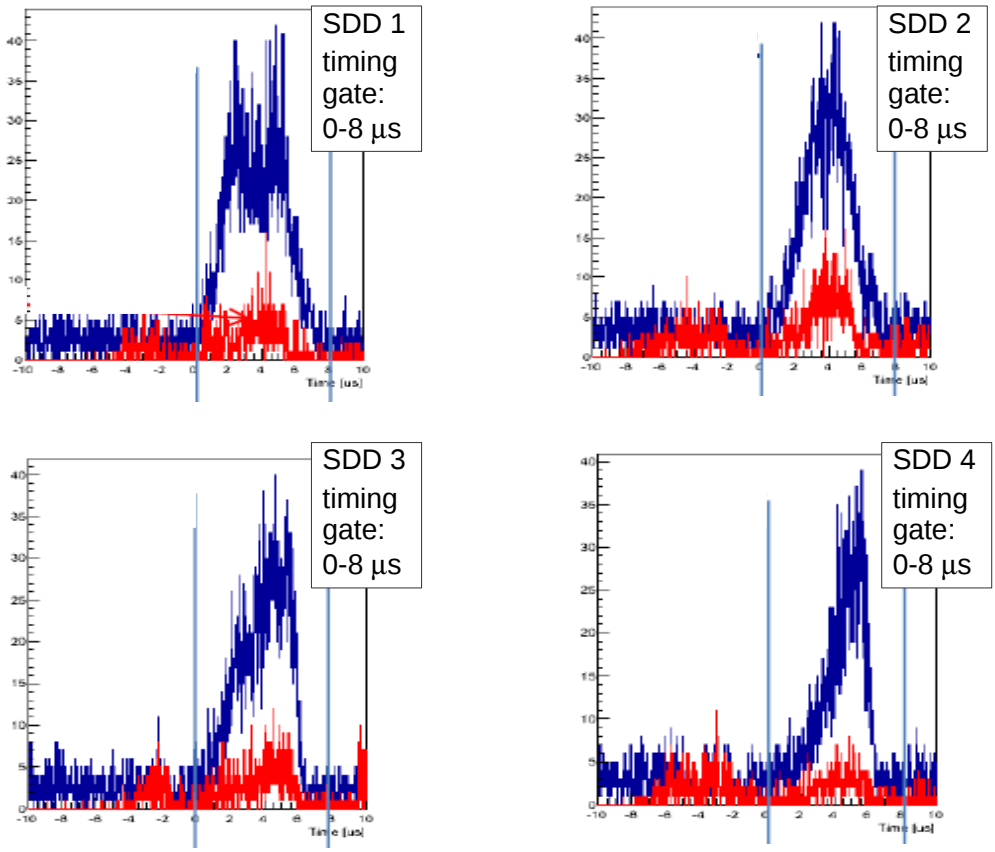

Figure 6.2: SDD1, SDD2, SDD3 and SDD4 beam timing analysis. The blue curve shows all events while the red curve shows events with Energy > 5 keV. The time gate used for the analysis is 8 μs.

The selection windows are defined using the sigma parameter of the gaussian functions used to fit the kaon peak. Different widths, corresponding to 6, 5 and 7 σ, of the selection window are set and for each one, a K^-Li spectrum is generated. The optimum dimensions are those which minimize the relative errors on shift and width parameter. In Fig. 6.4 (b) is shows a kaon selection using 6 sigma, which represent the optimum for our case.

In conclusion, the SDD timing cut reduces an important fraction of structured and continuous hadronic background, as well as part of the electromagnetic one.

An important improving in signal to noise estimation is coming from the reset cut, while the effect of E0 counter and BHD-T0 TOF selection is smaller than expected due to the partial removal of background by the SDD timing cut, already taken into account.

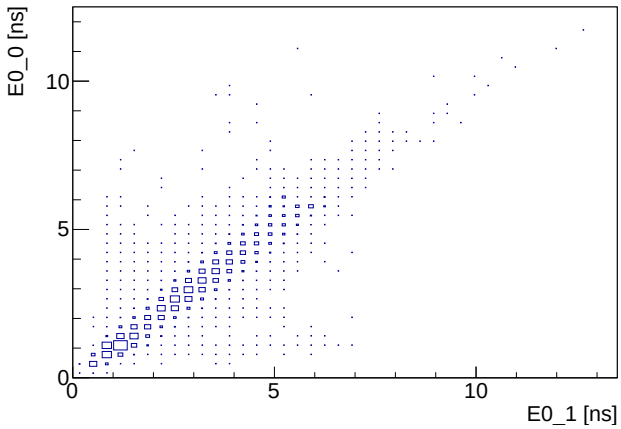

(a) correlation between E0(0) and E0(1)

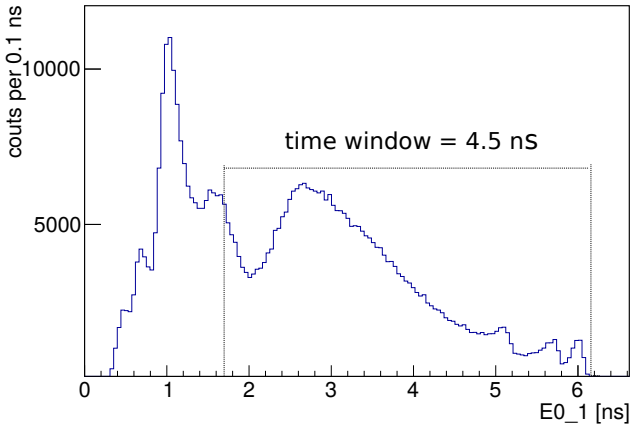

(b) E0(1) ToT

Figure 6.3: E0 time-over-threshold plots and time window selection. In order to remove the MIPs contamination, we selected only the kaon events which correspond to the peak between 1.7 ns and 6.2 ns.

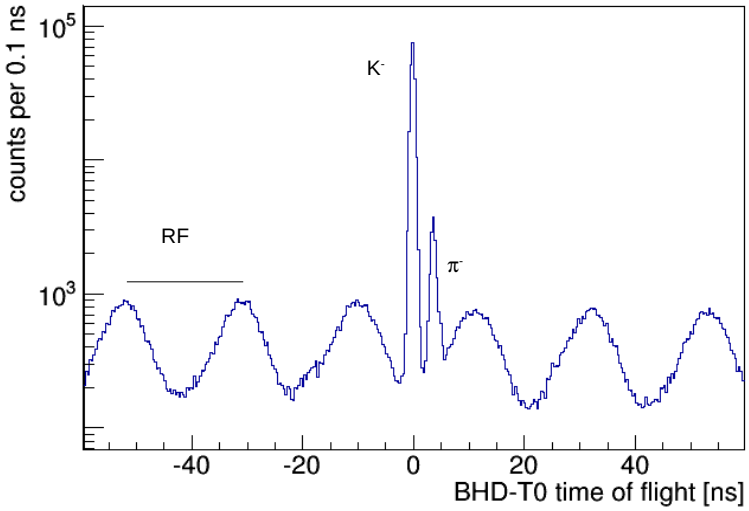

(a) BHD-T0 TOF

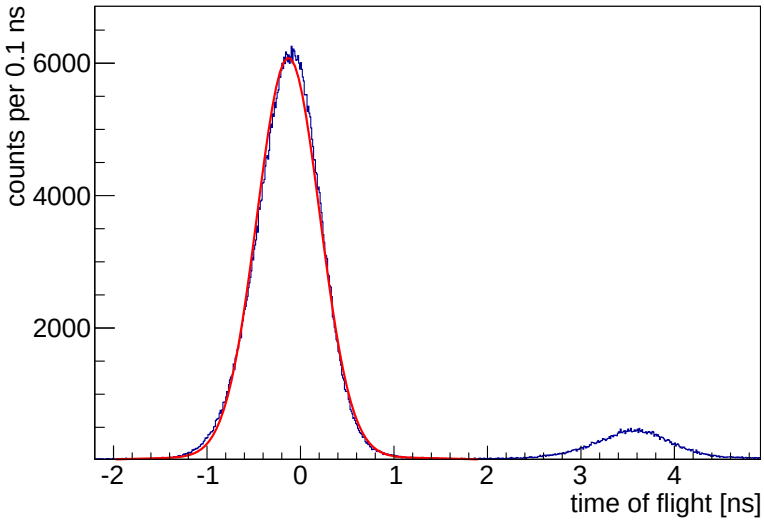

(b) kaon events selection (red)

Figure 6.4: kaons selection using time-of-flight (TOF) measurements between BHD and T0, scintillators counters at 7.7 m distance. The periodic structure underneath in (a) coming within one bunch from the radio frequency (RF). Kaons peak is centred at -0.13 ns and it's separated by 5.2 ns from pions peak. In (b) a kaon selection using 6 sigma (red), which represent the optimum dimensions in order to minimize the relative errors on shift and width parameter, is shown.

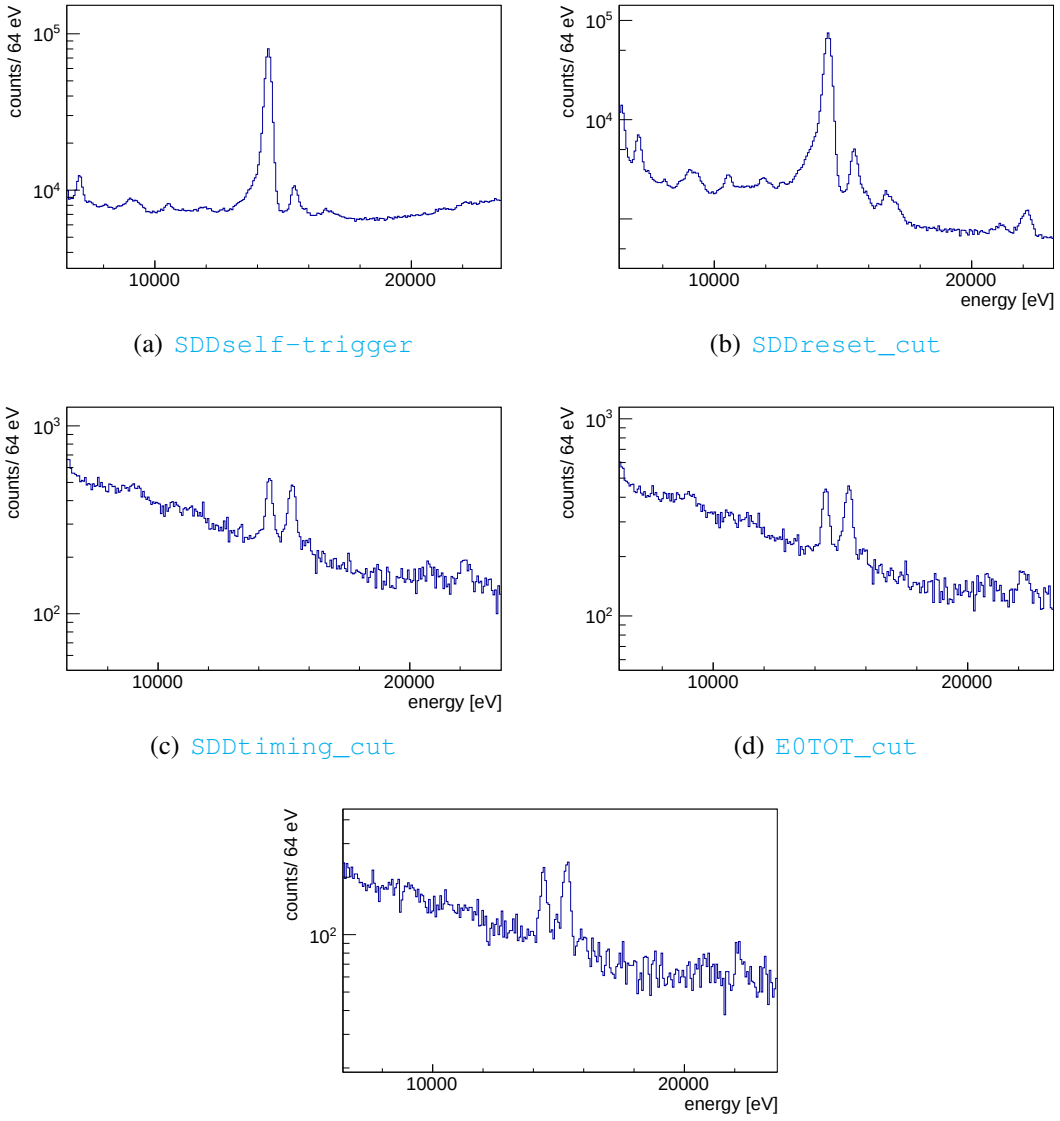

(a) SDDself-trigger

(b) SDDreset_cut

(c) SDDtiming_cut

(d) E0TOT_cut

(e) beam_cut

Figure 6.5: Common cut conditions. (a) select the events which made the SDD self-trigger, (b) SDD reset cut, (c) SDD timing cut, (d) E0 time-over-threshold cut (d) T0-BHD correlation cut.

6.3 Results

Once the cut conditions are optimized, the kaonic lithium spectrum is obtained, it has to be fitted in order to get values for the shift and width. The main fitting procedure characteristics are:

- Fit is performed in the energy range 11 < Energy < 20 keV in order to include $^{57}Co_{\gamma 1}$ and the Kaonic lithium L_α transition.
- In the energy range of interest, yttrium peaks are also present. Yttrium oxide is used in some ceramic for its low thermal expansion properties; it's a component of the ceramics on which the SDDs are mounted.
- All peaks included in the fit are listed in the table 6.2
- The kaonic lithium X-ray line was fitted by a Voig function which is the convolution of a Lorentzian line-shape with the detector response (see eq. 6.3).
- The $^{57}Co_{\gamma 1}$, yttrium $K_{\alpha 1}$ and $K_{\alpha 2}$ lines are fitted with multiple gaussian function.
- The yttrium $K_{\alpha 1}$ and $K_{\alpha 2}$ lines were fitted using fixed positions according to the table 6.2.
- All peaks have a fixed sigma calculated with parameters constant noise, ω and Fano factor coming from calibration, see eq. 5.1.
- Background is fitted with an exponential function.

Peak	Transition	Energy (eV)
$^{57}Co_{\gamma 1}$	$1 \rightarrow 0$	14412.95
$Y_{K\alpha 2}$	$2p \rightarrow 1s$	14882.94
$Y_{K\alpha 1}$	$2p \rightarrow 1s$	14958.54
$K^- Li_{L\alpha}$	$3d \rightarrow 2p$	15330

Table 6.2: Peaks included in the fit procedure. The theoretical energy value of a pure electromagnetic interaction $K^- Li_{L\alpha}$ is taken from [54].

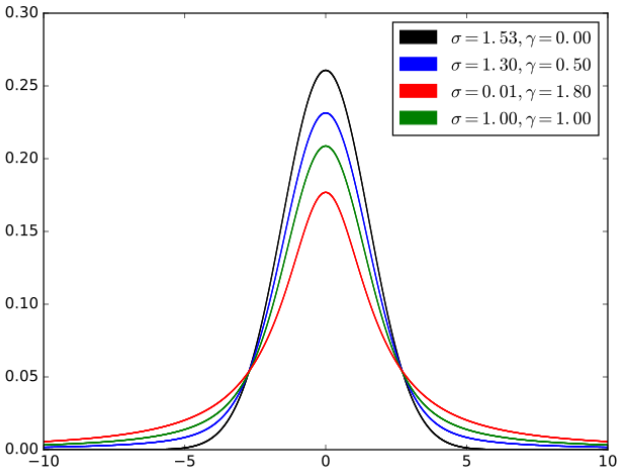

Figure 6.6: "Plot of the centered Voigt profile for four cases. Each case has a full width at half-maximum of approx. 3.6. The black and red profiles are the limiting cases of the Gaussian (γ =0) and the Lorentzian (σ =0) profiles respectively" [55].

The K^-Li transitions is fitted with Voigt function V(i, ε, Γ), defined as the convolution between a gaussian (G) and lorentzian (L) function:

$$V_K = V(X_K(i,\varepsilon), \sigma_K\Gamma) = \int_{-\infty}^{+\infty} G(x^{'}(i), \sigma_K) L(X_K(i,\varepsilon) - x^{'}(i), \Gamma) dx'(i) \tag{6.3}$$

where the $X_K(i,\varepsilon) = x_K^{EM} - \varepsilon(i)$ is the center of the peak related to the transition k and the σ_K is the standard deviation related to the k transition. The gaussian and the lorentzian function are defined as:

$$G(x'(i), \sigma) = \frac{\sqrt{2\pi}}{\sigma} e^{\frac{x'(i)^2}{2\sigma_K^2}} \tag{6.4}$$

$$L(X_K(i) - x'(i), \Gamma) = \frac{\Gamma}{2\pi} \frac{1}{(X_K(i,\varepsilon) - x'(i))^2 + \Gamma^2/4} \tag{6.5}$$

The parameter Γ related to the K^-Li transitions we want to determine is the natural line profile of the lorentzian function. The shift ε is defined as the difference between the K^-Li measured energy (E_{2p}) and the theoretical energy value of a pure electromagnetic interaction (E_{2p}^{EM}) (see table 6.1):

$$\varepsilon_{2p} = E_{2p} - E_{2p}^{EM} \tag{6.6}$$

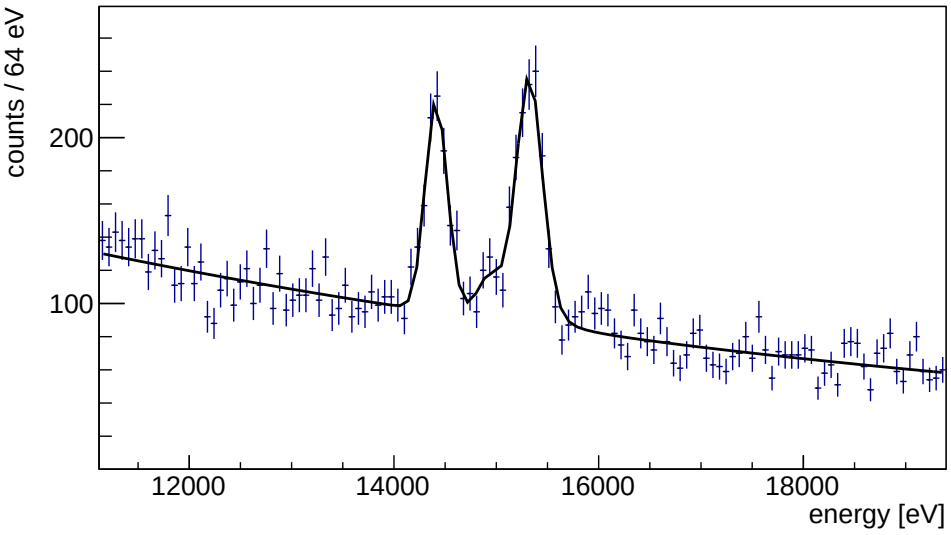

(a) ^{57}Co, Y and K^{-}Li fitted spectrum

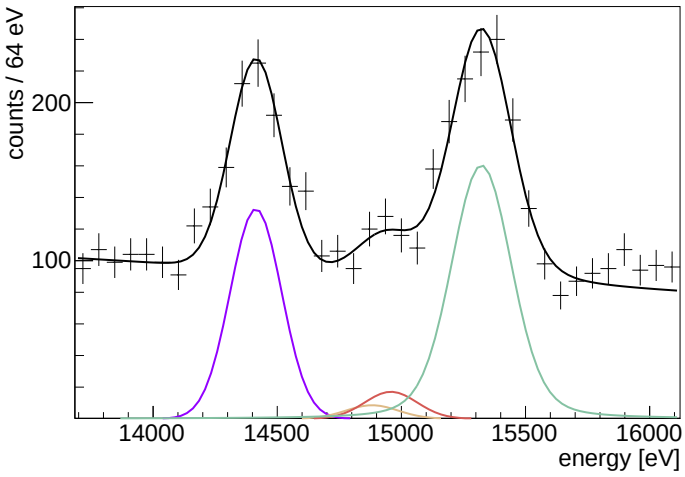

(b) Single peaks plot

Figure 6.7: ^{57}Co$_{\gamma 1}$ (blue), Y K$_{\alpha 1}$ and K$_{\alpha 2}$ (red and light red), Kaonic lithium (light blue) peaks and total fit (black) are shown.

The obtained chi-square is $\chi 2$= d.o.f: = 168.4/125 = 1.35. The results for the parameter ε and Γ are:

$$\varepsilon = (-7.5 \pm 5.4(stat))eV \tag{6.7}$$

$$\Gamma = (64.6 \pm 9.7(stat))eV \tag{6.8}$$

The number of K^-Li events used to the fit are 838. In table 6.3 the obtained parameters by the fit.

parameter	value	error
$entries$	54089	
χ^2/ndf	168.36/125	
$^{57}Co\ mean$	14414.97 (eV)	3.24 (eV)
$^{57}Co\ ampl.$	13717.06	1084.81
$K^-Li\ mean$	15322.51 (eV)	5.36 (eV)
$K^-Li\ ampl.$	53602.80	3930.99
$Y ampl.$	1792.84	137.70
b	$-0.1 \cdot 10^{-3}$	$0.1 \cdot 10^{-5}$
a	5.95	0.057

Table 6.3: The table shows the fit results for ^{57}Co, Y and K^-Li. *a* and *b* are the parameters of fit background.

6.3.1 Systematic errors evaluation on K^-Li shift and width

The data analysis of the K^-Li measurement is still on-going, a preliminary evaluation of the systematic errors on K^-Li shift and width is presented in this section. In table 6.4 different systematics errors are resumed. There are two main sources of systematic errors in this fit procedure. The first one is related to the rate correction and the linear function used to correct the final spectra.

A clear identification of the ^{57}Co position is a crucial point for a correct analysis of kaonic lithium spectra and systematic errors evaluation. The ^{57}Co is obtained with a shift of 2.02 eV from the theoretical value; this is the first systematic error on K^-Li shift to be included (tab. 6.4 (a)).

Another source of systematic errors is the eventual presence of some peaks so close to the K^-Li peaks that could modify the final value of the shift. In this case the Yttrium $K_{\alpha 1}$

and $K_{\alpha 2}$ transition respectively at 14958.54 eV and 14882.94 eV can influence the K^-Li shift and width measurement. In order to check this hypothesis fits with and without these peaks have been performed and results are shown in tab. 6.4 (b).

As pointed out in fig. 6.4 (b) in the previous section, the different widths of the kaons peaks in the BHD-T0 time of flight selection, are set and for each one a K^-Li spectrum is generated. The fit results for 5 and 7 σ of the selection window are summarized in tab. 6.4 (c).

At last, in the final analysis we used the mean values of Fano and constant noise parameters for all the SDDs considered. The associated systematic error was evaluated and the results were used to reanalyze the kaonic lithium spectra. The difference, respect to our final result, is evaluated as the related systematic error. The results are shown in tab. 6.4 (d).

	$\Delta\varepsilon(eV)$		$\Delta\Gamma(eV)$		
	plus	minus	plus	minus	
shift of ^{57}Co position	0.0	2.0	0.0	0.0	(a)
fit without Y peaks	2.5	0.0	5.1	0.0	(b)
5 σ TOF selection	0.8	0.0	5.4	0.0	(c)
7 σ TOF selection	0.4	0.0	5.4	0.0	(c)
use of mean Fano and c.noise parameter	1.2	0.9	4.2	1.0	(d)
TOTAL (added in quadrature)	3	2	9	1.0	(e)

Table 6.4: Resume of the different systematic error contributions on K^-Li shift and width.

Systematic errors of shift and width have been added as:

$$\delta_{sys} = \sqrt{a^2 + b^2 + c^2 + d^2} \tag{6.9}$$

In this chapter we have presented the results of the kaonic lithium measurement at J-PARC. For the shift ε and the width Γ we obtained:

$$\varepsilon = (-7.5 \pm 5.4(stat)^{+3}_{-2}(syst))eV \tag{6.10}$$

$$\Gamma = (64.6 \pm 9.7(stat)^{+9}_{-1}(syst))eV \tag{6.11}$$

7 Summary

The measurement of X-ray transitions coming from exotic atoms is a powerful experimental tool for the study of the strong interaction at low energy. In particular, in the strangeness sector, fundamental information are obtained from kaonic atoms especially from low Z atoms like hydrogen deuterium and helium.

The $\overline{K}N$ interaction close to threshold provide crucial information of the importance of the interplay between spontaneous and explicit chiral symmetry breaking in low-energy QCD. In this context the importance of the kaonic deuterium X-ray spectroscopy has been well recognized, but no experimental results were obtained up to now due to the difficulty of the measurement.

Kaonic deuterium transitions to the ground level, together with the kaonic hydrogen results obtained by the SIDDHARTA experiment, will provide the isospin dependent antikaon-nucleon scattering lengths.

The proposed experiment will provide the strong-interaction level shift and width of the kaonic deuterium 1s state with most stringent constraints on the antikaon-nucleon interaction, promising a breakthrough for this field.

The development of optimized SDDs for X-ray spectroscopy allowed the experimental investigation of the kaonic deuterium system. The high-quality of the kaon beams delivered by the K1.8BR line together with the high efficiency of the K1.8BR spectrometer and the use of stable and fast X-ray detectors like SDDs, makes the E57 setup to be one of the best performing apparatus for this kind of measurements.

In this work we presented the results of the Monte Carlo simulation for a kaonic deuterium X-ray spectrum, assuming 30 days of data taking with an X-ray detector of 246 cm^2 active area. The yield ratios of the K_α:K_β:K_{total} transitions were taken from the kaonic hydrogen data, with an assumed K_α yield of 10^{-3} for the gaseous target and 10^{-4} for the liquid target. For the strong interaction induced shift and width theoretical prediction were used: shift = -800 eV and width = 750 eV.

We have shown that for a 30 kW proton beam power with a momentum of 660 MeV/c about $4.5 \cdot 10^8$ kaons per day can be expected entering the degrader. Assuming this kaon

intensity and rejecting the kaon correlated background using various triggers cuts, it will be possible to achieve a signal to background ratio of 1:4 for the kaonic deuterium K_α-line.

Uncorrelated background is estimated to be negligible, since the unprecedented timing resolution of the new SDD electronics scheme reduces it to a marginal level.

Within 30 days of beam time, using a gas density of 5% LDD, we will be able to collect 1500 K_α events, which will allow a determination of the strong interaction induced shift and width of the 1s state of kaonic deuterium with a precision of 60 eV and 140 eV, respectively.

The experimental results obtained by E57 during the test beam at J-PARC have been discussed. The purpose of the beam commissioning was to show good control and understanding of the K^- stopping, to confirm the SDD operation under real beam condition and to prove the effectiveness of the MC calculation.

In addition a lithium target has been used for the X-ray measurement, in order to measure the shift and width of the $3d \rightarrow 2p$ transition.

In this work we have presented the results of the kaonic lithium analysis. For the shift ε and the width Γ we obtained:

$$\varepsilon = (-7.5 \pm 5.4(stat)^{+3}_{-2}(syst))eV \tag{7.1}$$

$$\Gamma = (64.6 \pm 9.7(stat)^{+9}_{-1}(syst))eV \tag{7.2}$$

List of Figures

2.1 Cascade process scheme for kaonic deuterium. 4

2.2 Real part (left) and imaginary part (right) of the $K^-p \rightarrow K^-p$ forward scattering amplitude extrapolated to the subthreshold region, deduced from the SIDDHARTA kaonic hydrogen measurement [7]. 11

2.3 Comparison of experimental results for the strong interaction shift and width of the kaonic hydrogen 1s state. 12

2.4 Example of a fit of kaonic deuterium X-ray lines. “X-ray spectrum from the kaonic deuterium experiment. Fit with fixed Kd transition shift and width (-805, 750 eV) and fixed yield ratio of the individual K-transitions. Integrated luminosity 100 pb^-1. The lines from kaonic X-rays due to stops in the window foils and from X-ray fluorescence excited by background are labeled" [30]. 13

2.5 Kaonic deuterium cascade calculations, for the X-ray yield of K_α, K_β, K_γ and K_{tot}; figure from reference [37] (left) and from [38] (right). 14

3.1 Configuration of the K1.8BR beam line in the hadron hall of J-PARC [40]. 16

3.2 Schematic view of the beam line spectrometer. The setup consists of a beam line spectrometer, a cylindrical spectrometer system (CDS), trigger counters (BHD and T0), beam line chambers (BLC1 and BLC2), and a kaon identification counter (AC). The beam line magnet, composed of an SQDQD system, consist of beam sweeping dipole magnets (D4 and D5), quadrupole magnets (Q7 and Q8) and a sextupole magnet (S3) [40]. . . . 17

3.3 E17setup. 18

3.4 E0 detector. The E0 detector consist of 3 segmented scintillator bars (EJ-230). Each segment has 30 mm (vertical) and 100 mm (horizontal) and 20 mm (thickness). Six PMTs, HAMAMATSU (6151-01B) are mounted on both ends of each scintillator. 19

3.5 Trigger counters. 20

3.6 E57setup at the K1.8BR. 21

3.7 “Monolithic array of eight 64 mm^2 SDD units. The ceramic carrier can be seen with holes to facilitate bonding of the SDD units and placement of charge pre-amplifiers (Top). The SDD array is mounted on a ceramic carrier which is further assembled on Aluminum holder with M1 screws (Bottom)" [41]. 22

3.8 Design of the cryogenic target and X-ray detector system. 23

4.1 Monte Carlo configuration of the E57 experiment (side view). The simulation covers the full focal point region, up to the T0 scintillator. The red tracks are kaons of 0.7 GeV/c momentum. 27

4.2 Same configuration with kaons of 0.7 GeV/c momentum in red, pion in green and muon in yellow. 27

4.3 Beam profile of the pions at T0 counter (130 cm upstream of final focus). The cross sections of perpendicular directions to the beam axis are shown (top). Position dependence of the momentum (bottom.) 29

4.4 The obtained 1.0GeV/c K^- yield and K^-/π ratio as a function of gap distance between the IF and the MS with an ES1 field of 50 kV/cm is shown.The K^- yield is normalized by a power of 1.0 kW (top). Measured kaon yields (Run 29 + Run 62) from 0.7 GeV/c to 1.1 GeV/c, normalised to the Run 62 data, recorded in April 2015 (bottom). 31

4.5 Kaon stopping distribution from degrader to target (left); kaon stops in the deuterium target(right). An additional prism-shaped degrader of carbon, in front of the main degrader, was used to compensate the position dependence of the momentum. Due to the hight momentum of the kaons a 40 cm degrader is needed in order to stop the particles into the target. As can be seen, 90% of kaons are stopped in the last 4 cm of the degrader and only $0.5{\cdot}10^{-3}$ per beam kaon into 5% (LDD) target. For the liquid case, $9.5{\cdot}10^{-3}$ per beam kaon are stopped into the target. 32

4.6 Simulated kaonic deuterium spectrum assuming an X-ray yield of 0.1%. Shift is -800 eV and a width 800 eV and . Almost 800 K_α could be collected, which leads to a precision of the fit result in this statistical sample of: 60 eV (shift) and 140 eV (width). The dashed line at 7834 eV shows the pure QED value of K_α. 34

4.7 beam tuning setup (side view). 36

4.8 Event vertex with the kaon beam reconstructed by the FDC1. The cross sections of perpendicular directions to the beam axis is show. 37

4.9 Event vertex with the kaon beam reconstructed by the FDC1. The cross sections of parallel directions to the beam axis is show. 37

4.10 energy deposit on E0 counter by K^- and K^+ beam depending on vertex position. 37

5.1 The schematic drawing of the Silicon Drift Detector (top). The SDD drift field, properly shaped as a conveyor (bottom) [46]. 41

5.2 3x3 matrix. Frontside (left); backside (right). 43

5.3 DAQ logic. Only the SDD unit 1 layout is shown completed as an example, the other 3 units follow the same logic. 44

5.4 Spectra of all the 24 channels acquired in a parallel acquisition. The energy resolution of the Mn-K_α-line of the ^{55}Fe calibration source is shown. Each column correspond to a single SDD array. The differences between channels are due to the different leakage currents. 45

5.5 Typical calibration spectra obtained with and without kaon beam. 47

5.6 ^{57}Co fit. Only Gauss and Tail were used for the fitting. 48

5.7 Stability of the ^{57}Co peak position. 49

5.8 Run summary. 51

6.1 Measured spectra obtained with Li (metal) and LiH target. The Li spectra was obtained with $2.7 \cdot 10^7$ kaons stopping in the target whilst for LiH the number of stopping kaons was $1.9 \cdot 10^7$ [53]. 53

6.2 SDD1, SDD2, SDD3 and SDD4 beam timing analysis. The blue curve shows all events while the red curve shows events with Energy > 5 keV. The time gate used for the analysis is 8 μs. 56

6.3 E0 time-over-threshold plots and time window selection. In order to remove the MIPs contamination, we selected only the kaon events which correspond to the peak between 1.7 ns and 6.2 ns. 57

6.4 kaons selection using time-of-flight (TOF) measurements between BHD and T0, scintillators counters at 7.7 m distance. The periodic structure underneath in (a) coming within one bunch from the radio frequency (RF). Kaons peak is centred at -0.13 ns and it's separated by 5.2 ns from pions peak. In (b) a kaon selection using 6 sigma (red), which represent the optimum dimensions in order to minimize the relative errors on shift and width parameter, is shown. 58
6.5 Common cut conditions. (a) select the events which made the SDD self-trigger, (b) SDD reset cut, (c) SDD timing cut, (d) E0 time-over-threshold cut (d) T0-BHD correlation cut. 59
6.6 "Plot of the centered Voigt profile for four cases. Each case has a full width at half-maximum of approx. 3.6. The black and red profiles are the limiting cases of the Gaussian (γ =0) and the Lorentzian (σ =0) profiles respectively" [55]. 61
6.7 $^{57}Co_{\gamma 1}$ (blue), Y $K_{\alpha 1}$ and $K_{\alpha 2}$ (red and light red), Kaonic lithium (light blue) peaks and total fit (black) are shown. 62

List of Tables

2.1 Compilation of predicted K^-d scattering lengths a_{k-d} and corresponding experimental quantities ϵ_{1s} and Γ_{1s} (taken from [36]). 12

3.1 Parameters of the K1.8BR beam line [40]. 16

4.1 sources of background. 28
4.2 "Kaon stopping density in gaseous and liquid targets, optimised for carbon degrader. The target density is given relative to the liquid deuterium density (LDD)" [42]. 30
4.3 Starting point for the evaluation of the background rates and the finally produced K_α events are the number of kaons per spill and kW at the beam counter T0 (taken from E57 Proposal for J-PARC 50 GeV Proton Synchrotron). This kaon number, to start with, is extracted from the E15 measurement in April 2015. 35
4.4 Comparison between MC results for kaon momentum of 0.7 GeV /c and 0.9 GeV /c, respectively first and second column and real data with a beam of 0.9 GeV /c last column. 35

5.1 Calibrations sources used during the E57 test beam. Revised November 1993 by E. Browne (LBNL). 46
5.2 Example of a fit results for calibration without kaon beam (SDD 1 ch 1). P0 and P1 are the linear background parameters, ω is the e-h pair creation factor, while slope is the conversion factor (ch/eV). 48

6.1 Strong interaction widths and shifts of K^-Li [53]. 54
6.2 Peaks included in the fit procedure. The theoretical energy value of a pure electromagnetic interaction $K^-Li_{L\alpha}$ is taken from [54]. 60
6.3 The table shows the fit results for ^{57}Co, Y and K^-Li. a and b are the parameters of fit background. 63

6.4 Resume of the different systematic error contributions on K^-Li shift and width. 64

181

Bibliography

[1] E. Fermi and E. Teller (1947) Phys. Rev. 72, 399-408.

[2] S. Tomonaga and G. Araki (1940) Phys. Rev. 57, 459-460.

[3] W.F. Fry (1951) Phys. Rev. 83, 594-597.

[4] T. Yamazaki (1995) Nucl.Phys. A 585(1-2), 215-223.

[5] J. Zmeskal et al., Nucl.Phys. A 790, (2007) 667c-670c.

[6] M. Däring, U.-G. Meißner, Phys. Lett. B 704 663 (2011).

[7] Y. Ikeda, T. Hyodo, W. Weise, Phys. Lett. B 706 63 (2011).

[8] U.-G. Meißner, U. Raha, A. Rusetsky, Eur. Phys. J. C 35 (2004) 349.

[9] S. Deser, M.L. Goldberger, K. Baumann, and W. Thirring (1954) Phys. Rev. 96, 774-776.

[10] C.J. Batty, Nucl. Phys. A 372 (1981) 418.

[11] C.B. Dover et al., Ann. Phys. 66 (1971) 248.

[12] J. Höfner et al., Ann. Phys. 73 (1972) 525.

[13] H. de Vries. At. Data Nucl. Data Tables 36 (1987) 495.

[14] M. Lutz et al., Nucl. Phys. A 574 (1994) 755.

[15] W.A.Bardeen et al., Phys. Rev. C 3 (1971) 1785.

[16] W.A.Bardeen et al., Phys. Lett. B 38 (1972) 135.

[17] M. Alberg et al., Phys. Rev. Lett. 30 (1973) 255.

[18] M. Alberg et al., Ann. of Phys. 96 (1976) 43.

[19] M. Thies, Phys. Lett. B 70 (1977) 401.

[20] M. Thies, Nucl. Phys. A 298 (1978) 344.

[21] W.Weise et al., Phys. Lett. B 64 (1976) 424.

[22] R. Brockmann et al., Nucl. Phys. A 308 (1978) 365.

[23] E. Friedman et al., Nucl.Phys. A 579 (1994) 518.

[24] C.J. Batty et al., Nucl. Phys. A 535 (1991) 548.

[25] G.E. Brown et al., Phys. Lett. B 291 (1992) 355.

[26] M. Iwasaki, et al., Phys. Rev. Lett. 78 (1997) 3067.

[27] G. Beer, et al., DEAR Collaboration, Phys. Rev. Lett. 94 (2005) 212302.

[28] Bazzi et al., Phys. Lett. B 704 (2011) 113.

[29] R.H. Dalitz et al., ed. by B. Povh (M.P.I., Heidelberg 1982), p. 201

[30] Bazzi et al., Nucl Phys. A. 907(100) 69-77 (2013).

[31] W. Weise, arXiv:1412.7838 [nucl-theo] (2015).

[32] T. Mizutani, C. Fayard, B. Saghai, K. Tsushima, arXiv:1211.5824[hep-ph] (2013).

[33] N.V. Shevchenko, Nucl. Phys. A 890-891 (2012) 50-61.

[34] A. Gal, Int. J. Mod. Phys. A 22 (2007) 226.

[35] U.-G. Meißner, U. Raha, A. Rusetsky, Eur. Phys. J. C 47 (2006) 473.

[36] M. Bazzi, et al., Nucl. Phys. A 907 (2013) 69.

[37] T.Koike, T. Harada, Y. Akaishi, Phys. Rev. C 53 (1996) 79.

[38] T. S. Jensen, Proceedings of DAFNE 2004: Physics at meson factories, (2004).

[39] J. Zmeskal et al., A Phys Pol B.46.101 (2014).

[40] K. Agari et al,. Prog. Theor. Exp. Phys. (2012) 02B011.

[41] C. Fiorini et al., IEEE transactions on nucl. science 60 4 (2013).

[42] J. Zmeskal et al., Proposal for J-PARC 50 GeV Proton Synchrotron (2014).

[43] E. Clyde et al., Phys. Rev. A 9 (1974) 6.

[44] E. Gatti, P. Rehak, Nucl. Instr. and Meth. A 225, 1984, pp. 608-614.

[45] Lechner et al., Nucl. Instr. and meth., 1996; A 377, pp. 346-351.

[46] P. Lechner, Nuclear Instruments and Methods in Phys. Research A 458 (2001) 281.

[47] G. W. Phillips, K.W. Marlow, Nucl. Instr. and Meth. 137 (1976) 525.

[48] J.L. Campbell, Nucl. Instr. and Meth. B 49 (1990) 115.

[49] J.A. Maxwell et al., Nucl. Instr. amd Meth. B 43 (1989) 218.

[50] J.A. Maxwell et al., Nucl. Instr. amd Meth. B 95 (1995) 407.

[51] J.L. Campbell, J.A. Maxwell, Nucl. Instr. and Meth. in Phys. Res. B 129 (1997) 297-299.

[52] B.G. Lowe and R.A. Sareen (2007) Nucl. Instr. Meth. A 576, 367-370.

[53] C. J. Batty et al., Nucl. Phys. A 282 (1977) 487-492.

[54] J. P. Santos et al., Phys. Rev. A 71 (2005) 032501.

[55] H. Di Rocco, A. Cruzado, Acta Phys. Polonica A 122 4 (2012) 666-669.